HOKKAIDO UNIVERSITY

Title	Effect of curing temperatures and additional activators on chloride ingress and its induced mineralogical alteration of ground granulated blast furnace slag activated by Ca(OH)2
Author(s)	Qi, Zhai; Zuo, Yibing; Kurumisawa, Kiyofumi et al.
Citation	Cement & concrete composites, 141, 105153 https://doi.org/10.1016/j.cemconcomp.2023.105153
Issue Date	2023-08
Doc URL	https://hdl.handle.net/2115/95154
Rights	© <2023>. This manuscript version is made available under the CC-BY-NC-ND 4.0 license https://creativecommons.org/licenses/by-nc-nd/4.0/
Rights(URL)	https://creativecommons.org/licenses/by-nc-nd/4.0/
Type	journal article
File Information	20230317no.pdf

Hokkaido University Collection of Scholarly and Academic Papers : HUSCAP

Effect of curing temperatures and additional activators on chloride ingress and its induced mineralogical alteration of ground granulated blast furnace slag activated by $Ca(OH)_2$

Qi Zhai [a, 1], Yibing Zuo [b, 1], Kiyofumi Kurumisawa [c, *], Aoran Lang [a]

[a] Division of Sustainable Resources Engineering, Graduate School of Engineering, Hokkaido University, Japan

[b] School of Civil and Hydraulic Engineering, Huazhong University of Science and Technology, Wuhan, China

[c] Division of Sustainable Resources Engineering, Faculty of Engineering, Hokkaido University, Japan

* Corresponding author: kurumi@eng.hokudai.ac.jp

[1] The first two authors contributed to this work equally.

Abstract

The impact of additional activators (sodium sulfate, sodium nitrite, and calcium nitrite) and curing temperature (20 and 35 °C) on chloride binding and ingress resistance of ground granulated blast furnace slag activated by $Ca(OH)_2$ was studied using X-ray diffraction, scanning electron microscopy, thermogravimetric and thermodynamic modeling. The outcomes of the study indicated that the difference in the chloride binding capacity at low chloride concentrations was primarily affected by the types of the AFm phase. The solid solution formed between Friedel's salt and various types of AFm phases resulted in a decrease in the chloride binding capacity. At a curing temperature of 35 °C, the chloride binding capacity reduced due to the leaching of calcium ions and carbonation induced by the coarse pore structure. It was found that the chloride ingress resistance was significantly related to the leaching of calcium and carbonation, and the denser calcite layer formed at the exposure layer had a positive impact on the chloride ingress resistance.

Keywords: Chloride binding, Chloride ingress resistance, Ground granulated blast furnace slag, Thermodynamic modeling, Additional activators

1. Introduction

In recent years, the widespread use of cement as a binder for concrete is limited due to sustainability issues [1]. A frequent concern with durability, which further causes structural deterioration and failure of concrete, is the chloride-induced corrosion of steel reinforcements [2-4]. The rising demand for cement and concrete has facilitated the development of eco-friendly alternatives to OPC such as alkali-activated materials (AAMs) in recent years [5–7]. There has been significant research on the use of industrial waste and by-products including fly ash, silica fume, metakaolin, and ground granulated blast furnace slag (GGBFS) in alkali activation systems [8–10]. Among these, alkali-activated slag (AAS) is the most commonly utilized AAM [11,12]. The AAS has a low carbon footprint, low heat of hydration, good chemical resistance, and high early mechanical properties [13,14]. Recent studies have also demonstrated that AAS has the ability to bind chlorides than OPC [15–17]. The commonly used activators for AAS are water glass and NaOH. However, the use of these activators can cause quick setting and toxicity to the environment. Waterglass can cause skin and eye

irritation if it comes into contact with the skin or eyes. Further, the production of sodium silicate can generate waste by-products, such as salt cake, which can be harmful to the environment if not disposed of properly. The NaOH is a strong alkaline substance that can cause burns and tissue damage if it comes into contact with the skin, eyes, or respiratory system [11,19–22]. $Ca(OH)_2$ is a more economical activator; furthermore, it can help initiate slag hydration in slag cement binders. Several previous studies have investigated the activating behavior of $Ca(OH)_2$, which showed $Ca(OH)_2$ have a similar activating efficacy to those of other activators commonly used in AAS binders [8,21,23]. However, the pH of $Ca(OH)_2$ activation is approximately 12.5, lower than the alkalinity (pH>13.0) required to promote slag dissolution [18]. Consequently, the initial dissolution rate of slag will be lower than that of systems using other alkali solution and thus lead to lower mechanical properties.

According to previous research, changing the curing conditions, such as increasing the curing temperature or adding an appropriate amount of additional activators, can promote the reaction of slag [24]. Snellings et al. [25] found that elevated curing temperature resulted in a decrease in the ettringite at the later ages of slag reaction. Osio-Norgaard et al. [12] observed the crossover effect at a curing temperature greater than 40 °C. This phenomenon made the pore structure coarser. Evidently, changing the reaction environment will directly affect the pore structure, pore solution composition, and hydrates assemblage, and this will have a subsequent impact on the chloride resistance of cementitious materials. Based on previous studies, a detailed impact of additional activators and curing temperature on the chloride resistance is discussed below:

Activators with different cations (Na^+, K^+, Mg^{2+}, etc.) have the most significant impact on the pH and ion concentrations in the pore solution. The addition of alkali metals (Na^+, K^+) will result in an increase in the pH value, and this may further accelerate the initial dissolution of slag. Accordingly, a higher number of hydration products are generated, and the porosity can be considerably reduced [26,27]. This means that the resistance to chloride ingress could be improved. For Mg^{2+}, although the pH of the initial pore solution is lower than that of other alkali activators [8,28], it is believed that in AAS, a hydrotalcite-like phase can be formed with a moderate MgO content when Al reacts with Mg. This phase may lead to a similar chloride binding capacity with AFm as that induced by the layered double hydroxide (LDH) structure with exchangeable interlayer spaces. Several studies have demonstrated the ability of the hydrotalcite-like phase to uptake chlorides [29–32]. However, a major challenge is that the quantity of this phase depends on the investigated system, and the exchangeable sequence of the anions could be ranked as $CO_3^{2-} > SO_4^{2-} > OH^- > F^- > Cl^- > Br^- > NO_3^- > I^-$. Thus, for a higher alkali content, hydrotalcites may preferentially react with CO_3^{2-} or SO_4^{2-} before chloride exchange occurs [12,32,33]. Chen et al.[32] discussed the potential of nitrate- or nitrite-intercalated hydrotalcite to enhance corrosion control. Although they highlighted the considerable potential of postponing corrosion initiation, chloride ingress may be enhanced due to the pore coarsening effect caused by an alteration in the pore structure. For activators with different anions, the most evident impact is the change in the AFm phase's ability to bind chloride. Chlorides can be chemically bound in the AFm phase in the form of Friedel's salts ($3CaO \cdot Al_2O_3 \cdot CaCl_2 \cdot 10H_2O$) and Kuzel's salts ($3CaO \cdot Al_2O_3 \cdot 0.5CaSO_4 \cdot 0.5CaCl_2 \cdot 11H_2O$) mainly due to the phase change caused by ion exchange [34]. The added anions, such as CO_3^{2-}, SO_4^{2-}, OH^-, NO_3^-, and NO_2^-, in the interlayer of the AFm-like phase

can change the structure, and this may further affect the polymorphs of Friedel's salt produced by AAS [16]. The AAS contains a high number SO_4^{2-} ions and possesses a relatively stronger chloride binding capacity due to the decomposition of ettringite (AFt) [35]. In addition, according to the chloride concentration, the pH value and the anion type in the solution, various solid solutions of Friedel's salt may be formed. However, Kuzel's salts seem to be unstable in the presence of carbonate [16,36,37]. When additional activators are applied to achieve a high pH environment, the most apparent negative impact is the increase in the leaching of calcium ions. Leaching may cause decalcification of C-(A)-S-H, and it may lead to a decrease in the physical bindings of chlorides in the C-(A)-S-H diffuse layer due to the higher competition with hydroxyl ions resulting from additional activators, indicating a decrease in the chloride binding capacity [37–39].

From the point of view of curing temperature, in general, 20 °C, which is a typical laboratory condition, is used as the reference temperature. Heat curing helps increase the reactivity required to reduce porosities and the average pore size of AAMs irrespective of the precursor. This may further result in an increase in the chloride binding capacity [12,40–43]. Osio-Norgaard et al.[12] investigated the impact of curing temperature in the range 20–38 °C on the chloride ingress resistance of a slag blended system, and they found that a higher curing temperature could result in an increase in the chloride binding capacity. They stated that the enhancement phenomenon is attributed to the accelerated reaction degree of slag. They also found that the pore structure became coarser at a curing temperature of 38 °C and aggravated chloride ingress. For AAS, although few studies have studied the impact of a higher curing temperature on the chloride binding capacity, numerous studies have analyzed the impact on the engineering properties [44–46]. Although a curing temperature greater than 20 °C can promote slag dissolution at an early stage, which further leads to the development of more rapid hydration products like (C-A-S-H gel), the thick shell of this hydration products surrounding the slag inhibits further slag hydration [44]. Moreover, thermal cracks may occur and increase the porosity, which may result in a decrease in the chloride ingress resistance [47].

Similar findings were observed in a previous study. Additional activators such as calcium nitrite ($Ca(NO_2)_2$ and sodium sulfate (Na_2SO_4), along with a high curing temperature (35 °C), promote slag hydration and make the pores finer at an early stage. However, at the later age, the porosity of samples to which activators have been added is larger than that of the specimens without additional activators, especially at a curing temperature of 35 °C, which suggests that the refinements in porosity are decelerated. Furthermore, in the $Ca(OH)_2$ activation, wherein calcium was added in the pore solution, additional $Ca(NO_2)_2$ could not effectively promote the slag reaction at early ages at ambient temperature, although the mechanical properties of this sample were significantly improved at later stages and were even comparable to those of the control group. However, at a high curing temperature, $Ca(NO_2)_2$ exhibits a finer porosity and higher reaction degree. This preliminary study showed that the reaction environment is crucial for the hydration process as well as to improve the long-term durability of slag activated by $Ca(OH)_2$. However, there is a lack of detailed characterization for the coupling effects of additional activators and high curing temperature on the chloride resistance. Thus, although the external reaction conditions are changed to improve the early performance, the comprehensive effect should be balanced against the

potential negative impact on the long-term performance or durability.

A majority of the results in the corresponding literature cover the chloride ingress resistance and binding capacity of the AAS system. There is a lack of information on the impact of additional activators and curing temperature on the durability performance in the slag activated by $Ca(OH)_2$ system in chloride-bearing environment. Therefore, the objective of this investigation was to study the chloride ingress and its induced mineralogical alteration of slag activated by $Ca(OH)_2$ at various reaction environments. The findings of this study will offer insights into the mechanisms of the chloride binding capacity and the chloride ingress resistance of slag activated by $Ca(OH)_2$ system that is exposed to sodium chloride, which could help broaden the practical applications of $Ca(OH)_2$ system.

2. Materials and methods

2.1. Materials and sample preparation

The chemical composition of the slag and calcium hydroxide investigated in this study have been described in previous studies [48] and are provided in Table S1. The particle size distribution of the materials used in this study is given in Fig. S1. A $Ca(OH)_2$/slag ratio of 0.2/0.8 and water/binder (slag+ $Ca(OH)_2$) ratio of 0.55 was used for mortars and pastes based on previous research [48]. For mortar, standard sand (specific gravity:2.64, water absorption:0.42%, fineness modulus: 2.93) with particle size in the range 0.08–2.0 mm according to the specification JIS R5201 was used, and the sand-to-binder ratio was set to 3.0. Additional activators were created by adding reagent-grade Na_2SO_4, $Ca(NO_2)_2$, and $NaNO_2$ to distilled water at a dose of 0.1 mol/kg of powder. Only deionized water was added to the samples as the control. The matrix of systems studied is shown in Table 1. The following steps were used to mix the pastes and mortars in a Hobart mixer: all solid components were combined for 30 s at low speed; the prepared activators were added, followed by mixing at a slow speed for 60 s, and a pause for 30 s to scrape down the binders on the sides of the bowl and blade. Next, mixing was performed for another 2 min and 30 s at high speed. After mixing, the paste was poured into Φ50 × 50 cylindrical plastic cups, and mortar was poured into cylindrical molds of Φ50 × 100 mm. The samples were sealed with polythene sheets and cured at temperatures of 20 or 35 °C for 28 days.

Table 1. Experimental matrix

Binders	Additional activators	Activator (wt% of binder)	Curing temperature
80% GGBFS+ 20% $Ca(OH)_2$	blank	/	20 °C
	blank	/	35 °C
	Na_2SO_4	1.42%	20 °C
	Na_2SO_4	1.42%	35 °C
	$Ca(NO_2)_2$	1.51%	20 °C
	$Ca(NO_2)_2$	1.51%	35 °C
	$NaNO_2$	0.69%	20 °C
	$NaNO_2$	0.69%	35 °C

Note: The name of the additional activators will be substituted for the name of the sample in the following exposition.

2.2. Properties before chloride immersion

2.2.1.Compressive strength

Before conducting the relevant experiments related to chloride attack, several properties of the samples were evaluated to demonstrate the impact of additional activators and curing temperature on the performance of $Ca(OH)_2$ activation. The strength test was performed according to the standard ISO 679.The mortars were demolded at an age of 3, 7, and 28 days for compressive strength measurement of three replicates. An automatic testing device (Hi-ACTIS-2000) was used to assess the compressive strength at a constant load rate of 0.4 N/mm^2·s.

2.2.2.Reaction degree

The selective dissolution method for analyzing AAS was adopted based on the description of Villagrán–Zaccardi et al. [49]. After being ground, the particle size of the samples was less than 125 μm. Then, the powder was dissolved in EDTA solution. The mixture was then filtered using a 2-μm filter paper after being agitated at 300 ppm for 2 h. Selective dissolutions were repeated twice for each mix. This method only left behind the unreacted slag and Mg-Al-OH as the residue.

2.2.3.Mercury intrusion porosimetry

Mercury intrusion porosimetry (MIP) was used to assess the impact of additional activators and curing temperature on the pore structure. In this investigation, MIP was carried out using Micromeritics Auto Pore V 9600 (Micromeritics) on roughly 1 g of the crushed paste material with a sieve size in the range 2–5 mm. The porosity was measured using a pressure of up to 420 MPa, and the Washburn equation was used to convert the pressure to the pore entry radius at a contact angle of 130°.

2.3. Chloride binding capacity

2.3.1.Chloride binding test

The chloride equilibrium test used in this investigation is similar to that described by Tang et al. [50]. NaCl solutions of 0.025, 0.05, 0.1, 0.25, and 0.5 M were prepared. After 28 days of curing, after being crushed, the pastes were run through a sieve with a sieve size in the range 2–5 mm. Then, 6.0-g paste particles were poured into a 100-mL plastic cup with 60-mL chloride-rich solutions and stored at ambient temperature till they reached absorption equilibrium.

After 2 months, the samples were separated, and the supernatants were collected for calculation of chloride adsorption. Before measurement, undiluted suspensions were introduced in the ion chromatograph, and the measured concentrations were compared to those of the standard solutions to select the appropriate dilution times. The selected dilution times are shown in Table S2. Ion chromatography was used to measure the chloride

concentration (ICS-90, DIONEX, Sunnyvale, CA, USA). The total and free chloride content was calculated by Eq. (1):

$$Cl_b = (Cl_0 - \frac{Cl_{free}}{f}) \times \frac{V}{m} \quad (1)$$

where Cl_b is the bound chloride (mol/g of dry paste), Cl_0 is the initial chloride concentration in mol/L, Cl_{free} is the chloride concentration of the solution after dilution in mol/L, f is the dilution times, V is the volume of solution in mL, and m is the sample mass in grams.

The separated samples were submerged in acetone for 2 h to stop the reaction. The samples were then turned into powder in a ball mill and kept in vacuum conditions before X-ray diffraction (XRD) analysis.

2.3.2. XRD

Following the chloride binding test, the powdered specimens were examined by X-ray diffractometry (Multiflex, Rigaku) with Cu-K radiation at voltage and current of 40 kV and 40 mA, respectively. To analyze the crystalline phases, the specimen was scanned between 5° and 70° (2θ) with a step size of 0.02°. A scan time of 0.67 s per step was used. To quantify the amorphous phase, around 20% α-Al_2O_3 was used as the internal standard, and Profex was used to quantify the hydrates [51].

2.3.3.Thermodynamic modeling

The Gibbs free energy minimization program was used to investigate phase assemblages and chemically binding chloride of slag activated by $Ca(OH)_2$ with additional activators and different curing temperatures. The database Cemedata 18 was adopted as the main database, and the CNASH_ss model and MgAl-OH-LDH_ss were also used. The extended Debye-Huckel equation was used in this study. The ideal gas equation of state was used for the gaseous phase model. The formation of gibbsite, thaumasite were suppressed as it was unlikely that they formed at ambient environments. As reported in previous studies, chloride ions may not only be physically bound but also chemically bonded in hydrotalcite-like phases in AAS [31]. Therefore, a new solid solution model of MgAl-Cl-LDH_ss based on MgAl-OH-LDH_ss proposed by Zuo [53] was used in this investigation. The corresponding thermodynamic parameters are listed in supplementary data, and a detailed calculation procedure is shown in Ref. [53]. During simulation, a chemical equilibrium was assumed in the system.

As the base mix, 80 g slag, 20 g $Ca(OH)_2$, and the corresponding additional activators were utilized to simulate the chloride binding process. The hydration degree of the binders based on selective dissolution was adopted.

2.4. Chloride ingress resistance

2.4.1.Chloride diffusion test

After 28 days of curing, mortars were demolded and cut into half with a height of ~50

mm. After cutting, epoxy resin was applied to all surfaces except the sawn surface. The samples were cured at 20 °C overnight. After hardening, the sealed samples were immersed in saturated $Ca(OH)_2$ for 24 h to facilitate saturation to suppress the impact of capillary suction. Then, the specimens were immersed in 0.5 M NaCl for 28 days.

After exposure, one of the samples were cut in half parallel to the direction of the chloride ingress. Then, one small slice of the sample was cut off along the center area aligned to the exposed surface from one of the samples cut in half. The slice was embedded in acrylic resin that did not contain chlorine, followed by polishing and carbon coating for scanning electron microscopy (SEM) analysis to analyze the chemical composition of hydration products after chloride diffusion. The SEM was carried out with a JEOL JSM-IT200 operated at an accelerating voltage of 10 keV combined with an energy-dispersive spectrometer (EDS) at a 15 keV operating voltage and a working distance of 10 mm. The frames with $\times 2000$ magnification for EDS investigation were obtained. For analysis, the depth intervals were set as 0-1, 1-2, 2-3, 3-4, 4-5, and 5-7 mm, and the center part was set as the standard based on the results of the pre-determined colorimetric test of spraying silver nitrate. At least 25-point analyses at different depths and not less than 180 points in total for one sample were collected.

The other half of the specimens cut in half was further cut into a 40-mm long, 30-mm wide, and 5-mm thick slice, which was used for electron micro probe analysis (EPMA). The remaining specimen was used for making powder samples. The powdered samples were extracted from a range of depths below the exposed surface using a profile grinder, and they were stored in a vacuum bag for further analysis.

2.4.2. EPMA

For EPMA (wave dispersive spectrometer), the slice was embedded in acrylic resin and polished. The polished specimens were vacuum dried for three days and carbon coated before the EPMA test (JAX-8530F). The measurement conditions included a 15-kV accelerating voltage and 50-nA beam current. The apparent chloride diffusion coefficient and surface concentration were obtained based on Fick's second law [52]:

$$C(x,t) = C_s - (C_s - C_0)erf\left(\frac{x}{2\sqrt{D_c t}}\right) \quad (2)$$

where $C(x,t)$ is the chloride concentration at depth x (m) and time t (s), C_s and C_0 are the chloride concentration at the surface and the initial chloride concentration in wt%, respectively, x is the distance from exposed surface (m), D_c is the diffusion coefficient (m^2/s), and erf is the error function.

2.4.3.TGA

The powdered samples from 0-1, 2-3 mm, and center grinding layers were used for thermogravimetry analysis (TGA) analysis (Hitachi TG7000 instrument). About 12 mg powder was weighed and placed into a platinum crucible. The measurement was heated in the range 30–1000 °C at a rate of 10 °C/min with nitrogen flow.

3. Results

3.1. Properties before exposure to NaCl

Fig. 1 shows the compressive strength of the mortars at specified ages. At three days, the incorporation of additional activators helped improved the strength development, irrespective of the curing temperature. The Na_2SO_4 sample exhibited the highest strength, which is 7.9 MPa at 20 °C. The strength of the respective samples improved as the curing temperature increased, but the impact of additional activators was not as significant as that at 20 °C. The higher compressive strength may be attributed to the higher reaction degree, as shown in Fig. 2. However, at 28 days, compared to the control group, most additional activators had a negative impact on the strength development, especially Na_2SO_4, regardless of the curing temperature, which was similar to the results reported by previous studies [29,32]. As presented in Fig. 3 and Table 2, the low compressive strength was attributed to the coarsen pore structure.

Fig. 2 shows the reaction degree of the pastes at 3, 7, and 28 days. Generally, at an early stage, additional activators and a curing temperature of 35 °C significantly promoted the reaction of slag, and this is consistent with the results of strength development. However, when the curing age was raised to 28 days, the reaction degree did not seem to increase further.

The information of pore structure of the pastes at 28 days is presented in Fig. 3 and Table 2. To distinguish between the capillary pore and gel pore, the critical pore radius of 10 nm was used [54]. The total porosities of all the samples were similar, irrespective of composition the curing conditions. However, the samples that included additional activators had a larger fraction of capillary pores, and this phenomenon was aggravated at a high curing temperature.

Fig. 4 shows the XRD results between 5 to 35 °2θ of the pastes at 28 days. As the main hydrates in AAS[55], C-(A)-S-H and hydrotalcite-like phases were present in all samples. The additional activators had a considerable impact on the AFm phase. For Na_2SO_4, monosulfoaluminate (SO_4-AFm) and a small amount of ettringite (AFt) is clearly visible. For $NaNO_2$ and $Ca(NO_2)_2$, a broadening peak around 11.5° 2θ was detected. The solid solution of NO_2-AFm ($Ca_4Al_2(OH)_{12}(NO_2)_2{\cdot}4H_2O$) (basal spacing d = 7.91 Å) and hydroxy AFm (C_4AH_{13}) (basal spacing d = 7.99 Å)[56] was inferred. In addition, Mg–Al LDHs at 11.6° and hemicarboaluminate ($C_4Ac_{0.5}H_{12}$) at 10.5° were also detected. The identifying peak for $NaNO_2$ is broader than that of $Ca(NO_2)_2$ at 20 °C. The peaks are narrower but still slightly asymmetric at 35 °C. The amount of hemicarboaluminate varied according to the curing and storage conditions; the peak corresponding to hemicarboaluminate can be clearly observed in the control group at 20 °C, while the peak cannot be observed for other samples and the control cured at 35 °C.

In summary, a curing temperature of 35 °C and the additional activators could effectively improve the reaction and compressive strength at an early stage. However, the impact at the later stage was not significant. The samples with additional activators coarsen the pore structure and inhibit strength development at later ages.

Table 2. Porosity of the pastes at 28 days.

Sample ID	Total porosity	Gel pore proportion (Gel porosity)	Capillary pore proportion (Capillary porosity)
Con 20 °C	44.47 %	51.13% (22.74 %)	48.87% (21.73%)
Na_2SO_4 20 °C	42.95 %	40.61% (17.44%)	59.39% (25.51%)
$NaNO_2$ 20 °C	43.75 %	40.99% (17.93%)	59.01% (25.82%)
$Ca(NO_2)_2$ 20 °C	44.41 %	43.80% (19.45%)	56.20% (24.96%)
Con 35 °C	43.86 %	47.25% (20.72%)	52.75% (23.14%)
Na_2SO_4 35 °C	44.20 %	37.98% (16.79%)	62.02% (27.41%)
$NaNO_2$ 35 °C	47.02 %	39.62% (18.63%)	60.38% (28.39%)
$Ca(NO_2)_2$ 35 °C	43.52 %	41.43% (18.03%)	58.57% (25.49%)

3.2. Chloride binding isotherms

The results of the total chloride binding after equilibrium were estimated from the differences in the concentration of the exposure solution before and after equilibrium with samples of known mass. To evaluate the chloride binding isotherms, chloride binding values were fitted by Langmuir $C_{b,L}$ and Freundlich equation $C_{b,F}$ to evaluate which isotherm can better describe the chloride binding behavior, as shown in the following equations [17]:

$$C_{b,L} = \frac{\alpha_L C_f}{1+\beta_L C_f} \quad (3)$$

$$C_{b,F} = \alpha_F C_f^{\beta_F} \quad (4)$$

where C_b is the bound chloride, C_f is the free chloride after equilibrium, and α and β are the fitting parameters.

As shown in Fig. 5, the increase in chloride concentration by up to 0.5 M results in a subsequent rise in the quantity of bound chloride in all samples. In pastes equilibrated at 0.5 M NaCl, the bound chloride concentration varies from 13.8 to 21.7 mg/g, which is higher than both OPC and AAS with comparable liquid-to-solid mass ratios observed in data from Refs. [17,50,57–60]. Among these samples, the ones with added nitrites show strong chloride binding capacity, while those with added Na_2SO_4 show the lowest binding capacity. It is worth noting that the samples cured at 28 days show a similar reaction degree of slag, which indicated that the binding capacity of the pastes is significantly affected by other factors such as the type of hydration products and pore structure.

The chloride binding isotherms of the pastes fitted by Langmuir and Freundlich isotherms are shown in Fig. 6 using experimentally determined data points. Table 3 shows a list of the fitting parameters. The samples with added nitrites show a similar chloride binding, which is

higher than those of the control and Na_2SO_4 samples, especially when the initial chloride concentration reaches 0.5 M, which is similar to the chloride ion content in seawater. The Na_2SO_4 samples exhibited the weakest adsorption capacity of chloride ions. Compared to those of the specimens cured at higher curing temperature, a majority of the samples cured at 20 °C showed a higher chloride binding capacity.

Table 3 shows the fitting parameters of the Langmuir and Freundlich equations. The Freundlich equation provides a better fit for the data, as seen in Table 3. Hence, it was used to determine the chloride binding coefficient α in this study. The coefficients do not have any physical meaning as they are not material properties but can be used to indicate the chloride binding capacities of the samples. The chloride binding coefficient α was greater for the samples with added nitrites and those cured at lower temperatures.

Most studies have reported that the higher curing temperature could result in an increase in the chloride binding capacity of the samples due to the higher reaction degree, which further led to an increased amount of related hydration products [43]. However, the phenomenon was reversed in this study, which could be affected by the pore structure, pore solution composition, leaching phenomenon, and the dissolution of the chloride binding phase, and this should be assessed further.

Table 3. Fitting parameters for the Langmuir and Freundlich isotherms.

Sample ID	α_L	β_L	R^2	Model
Con 20 °C	144.23	5.99	0.99	Langmuir
Na_2SO_4 20 °C	87.17	4.24	0.99	
$NaNO_2$ 20 °C	286.46	12.97	0.98	
$Ca(NO_2)_2$ 20 °C	278.25	11.92	0.93	
Con 35 °C	132.60	5.77	0.99	
Na_2SO_4 35 °C	46.06	1.50	0.98	
$NaNO_2$ 35 °C	133.37	5.00	0.92	
$Ca(NO_2)_2$ 35 °C	267.60	11.86	0.99	
	α_F	β_F	R^2	
Con 20 °C	26.01	0.49	0.97	Freundlich
Na_2SO_4 20 °C	20.75	0.55	0.99	
$NaNO_2$ 20 °C	25.99	0.37	0.97	
$Ca(NO_2)_2$ 20 °C	27.47	0.39	0.99	
Con 35 °C	21.45	0.71	0.99	
Na_2SO_4 35 °C	18.94	0.38	0.99	
$NaNO_2$ 35 °C	28.27	0.52	0.97	
$Ca(NO_2)_2$ 35 °C	26.33	0.38	0.98	

3.3. Phase transformation after chloride binding test

The analysis of XRD patterns is presented in Fig. 7 and 8. The trend of phase transformation after chloride exposure was consistent for different samples, irrespective of the curing conditions. As shown in Fig. 7(a) and Fig. 8(a), as the chloride ion concentration increased, the amount of portlandite decreased and that of calcite increased, especially at

higher concentrations (i.e. 0.25 and 0.5 M).

The variation in the peak that was located between 10 and 12° (2θ) is more complex. The enlarged representative XRD patterns of samples after exposure to low and high concentrations of chloride are shown in Fig. 7 (b) and Fig. 8 (b), respectively. At low chloride concentrations, the peaks decreased to lower 2θ values, the peak intensities were low, and the peaks were broad, especially for the control group and Na_2SO_4. For the control group and Na_2SO_4, the peak around 11. 54° (2θ) was still visible, and a second peak appeared at approximately 11.04° (2θ), which was between those for hemicarboaluminate and Friedel's salt. As reported by Chen et al. [32] and Georget et al. [61], this peak may be associated with the solid solution of hemicarboaluminate and Friedel's salt. The exchange of CO_3^{2-} and Cl^- in the interlayer of the AFm-like phase resulted in an increase in the d-spacing. For $Ca(NO_2)_2$ and $NaNO_2$, a more symmetrical peak occurred around 11.14 ° (2θ), and this may be attributed to the higher anion intercalation rate provided by NO_2^- and easier exchange of NO_2^- with Cl^- [62]. At higher chloride concentrations, a more asymmetrical peak was observed around 11.2° (2θ) for all samples, which could be attributed to the decomposition of hemicarboaluminate and hydrotalcite-like phases. This will be explained in detail via thermodynamic modeling.

Fig. 9 presents the quantified XRD results of the samples after chloride exposure. The amount of Friedel's salt in all samples tended to increase gradually as the chloride ion concentration increased, and the amount of portlandite gradually decreased. The amount of hydrotalcite-like phase tended to slightly decrease, and the amount of hemicarboaluminate remained essentially unchanged. It is worth noting that as shown in Fig. 7 and 8, the changes in portlandite and hemicarboaluminate can only be used as a reference because portlandite reacts with carbon dioxide, thus producing large amounts of calcite. It seems that samples after chloride exposure are more easily carbonated, and this behavior was consistent with the phenomenon observed by Chen et al [32]. In addition, Buenfeld et al. [40] also observed some aragonite formed after chloride exposure.

3.4. Thermodynamic simulation of phase assemblages after chloride exposure

Fig. 10 shows the volume of the different hydration phases of the samples cured at 20 °C predicted by thermodynamic modeling. Due to the similar change tendency, the results for samples that were cured at 35 °C are displayed in the supplemental data. It is worth noting that the thermodynamic simulation predicts the results under ideal conditions, and thus, a comparison of the XRD results shows that almost no calcite is produced. Furthermore, the physical binding of C-(A)-S-H was also not considered in the thermodynamic simulation. However, it can still provide useful information regarding chemical chloride binding analysis and theoretical total chloride binding calculations.

When the chloride concentration increased, a majority of the AFm-like phase and portlandite gradually decomposed. In the control group, due to the lack of the SO_4-AFm phase, the C_3AH_6, hemicarboaluminate, and hydrotalcite-like phases started to transform into Friedel's salts. After complete decomposition of hydrotalcite, Friedel's salts continued to grow and brucite formed due to the release of Mg^{2+} from the hydrotalcite-like phase.

In Na_2SO_4, $NaNO_2$, and $Ca(NO_2)_2$, the situation was more complex due to the diversity of the AFm-like phase, especially at low chloride concentration. In these samples, before the

formation of Friedel's salt, Kuzel's salt ($Ca_4Al_2(OH)_{12}Cl(SO_4)_{0.5}(H_2O)_6$) were formed, and this is related to the SO_4-AFm phase that was formed before exposure to NaCl. As the Cl concentration increased, Kuzel's salts were transformed into Friedel's salts, and the released sulfates were bound in AFt when the chloride concentration was higher than 0.2 M. This finding is in agreement with the results of [63,64]. It seems that AFt recrystallizes in all the samples with additional activators. This behavior was not seen during the XRD measurement, and this may be attributed to the small amount of phase, which was not detectable. Evidently, in Na_2SO_4, more Kuzel's salts were formed due to the formation of more SO_4-AFm by the additional SO_4^{2-}. The formation of Kuzel's salts resulted in a decrease in the chloride binding capacity of the samples at a low concentration of NaCl, especially for Na_2SO_4, which can partially explain the low chloride binding capacity of Na_2SO_4 shown in Fig. 6.

Moreover, in all samples, the hydrotalcite-like phase decomposed and chloride-bearing hydrotalcite was not predicted to form in in environments with NaCl exposure, which is in agreement with the experimental results of Ke et al. [31] and the simulation results of Zuo et al. [53]. Among the decomposed hydrates, hemicarboaluminates seem to be more stable, and this may be related to the natural carbonation process. In addition, a more recent article [61] provides interesting insights into the interactions between CO_3-AFm and Friedel' salts. Hemicarboaluminate can accept anions such as chloride and sulfate to stabilize the solid solutions due to ion exchange, resulting in an increase in the configurational energy.

3.5. Element map and microstructure change after chloride diffusion

As a more pronounced calcium-rich layer was observed on the exposed surface in the samples that were 35-°C-cured, the elemental map of the samples after chloride exposure cured at 35 °C is presented in Fig. 11. The results of the 20-°C-cured specimens are displayed in the supplemental data. The precipitation of the calcium-rich layer, which is assumed to be made of carbonates (see Fig. 12), possesses a higher number of samples with added Na_2SO_4 and $NaNO_2$ (around 0.01 mm) than that in the control group and in samples with added $Ca(NO_2)_2$. The evidence for the calcium-rich layer being made of carbonates is given in Section 4.2 (Fig. 18). In all samples, except the unreacted slag, the Ca ions were uniformly distributed in the pores.

To further investigate the microstructural changes caused by chloride exposure, the backscattered electron (BSE) images of the 35-°C-cured samples are presented in Fig. 12. A typical microstructure observed in slag with $Ca(OH)_2$ activation is shown in Fig. 12(a). In addition to the large amount of unreacted GGBFS on the rims of hydration products, large amounts of agglomerated portlandite can be observed. However, after exposure, clusters of portlandite could not be clearly seen in the other samples except for the ones with added Na_2SO_4 (Fig. 12(c)). Instead, many calcium-rich phases were dispersed and filled in the pores, typically in $Ca(NO_2)_2$ (Fig. 12(e)), and this is in good agreement with the element map results. In Na_2SO_4, only the agglomerated portlandite remained. As mentioned previously, numerous filamentous hydration products assumed to be calcite were formed, as shown in Fig. 12(a) and (d). This was in good agreement with the XRD results (Fig. 8). The chemical composition and chloride binding capacity of the rims surrounding unreacted slag were analyzed by EDX, as shown in Fig. 12(b). The intermixed hydration products of the hydrotalcite-like phase and C-(A)-S-H were observed, and this was in good agreement with the results observed by Li et

al.[65] As demonstrated by numerous researchers, the physical binding contributed to a majority of the chloride binding capacity of the hydrotalcite-like phase and C-(A)-S-H. Compared to Cl-AFm shown in Fig. 12(c), the binding capacity of the intermix hydration products was weaker. Fig. 12(c) shows the microstructure of Cl-AFm, which is assumed to be Kuzel's salt or the solid solution of Kuzel's and Friedel's salts. The observation is consistent with those of thermodynamic modeling. The Cl-AFm phase shows a sheet-like structure with a crack in the middle. A similar microstructure was reported in [66] in the case of SO_4-AFm, and it seems that Cl-AFm did not have a significant impact on the morphology of SO_4-AFm.

In cement-based materials, chlorides are bound chemically or physically in the hydration products, and it is believed that the chemical composition is affected. A detailed explanation of the change in the composition is given in the next section.

3.6. Characterization of changes in phase composition after chloride exposure

The EDX point analysis was performed on the samples after NaCl exposure. Fig. 13 shows the atomic ratios of Al/Ca versus Si/Ca. The composition of C-(A)-S-H was defined at edge of the cloud of C-(A)-S-H points, which represents the least intermixed points. The points near the tie lines correspond to a binary mixture [37].

As shown in Fig. 13, the Si/Ca ratio of C-(A)-S-H was in the range 0.3–0.7 for all the samples cured at 20 and 35 °C. This range is smaller than 0.4–0.8 and closer to that of the calcium-rich phase, which may be caused by the dissolution of calcium from portlandite, as suggested by XRD and BSE. Compared to the 20-°C-cured samples, the points of 35-°C-cured samples were more decentralized, and the cloud of C-(A)-S-H shifted relatively to the left and higher Al/Ca around 0.6 was found near the tie line corresponding to the AFm phase and C-(A)-S-H as presented in Fig. 12(b).

In Fig. 14, the atomic ratio of Mg/Si versus Al/Si is plotted to analyze the changes in the hydrotalcite-like phase. After chloride exposure, the change in Mg/Si versus Al/Si near the exposure surface was relatively less compared to the center area of the samples. However, two trends were observed for each of the temperatures. For the points obtained between 0 and 1 mm in depth, the distribution of data tended to be more linear. The average Mg/Al ratios observed at the main trends, which represent the hydrotalcite-like phase in this study, for the 20- and 35-°C-cured samples were 1.46 and 1.6, respectively. Evidently, both were lower than those of the pure hydrotalcite phase, which has a Mg/Al ratio from 2 to 3, as reported by Mill et al. [67]. As all the Mg in the hydrotalcite-like phase came from slag and most of the hydrotalcite-like phase formed surrounded unreacted slag, the lower Mg/Al ratio indicates intermixed phases of the hydrotalcite-like phase and C-(A)-S-H, as shown in Fig. 12. This was also supported by the Al/Si ratio shown in this figure and Fig. 12, wherein it was shown that the Al/Si exceeds the restricted Al/Si ratio, which is around 0.15, in synthetic C-(A)-S-H [68].

To identify the phases binding chloride, the Al/Ca versus Cl/Ca ratio is plotted in Fig. 15. For the 20-°C-cured samples, the highest Cl/Ca ratio, around 0.4, was obtained at depths of 0–2 mm, which may present the solid solution of Friedel's and Kuzel's salts. This agrees well with the results of thermodynamic modeling (Fig. 10) and BSE observations (Fig. 12). A favorable trend observed was that the Cl/Ca ratio decreased as the exposure depth increased.

For all samples cured at 20 °C, the Cl/Ca ratio converged to 0 at the depth from 4 mm. However, for samples cured at 35 °C, the highest Cl/Ca ratio was lower than 0.25, and this may be attributed to the solid solution of the hydrotalcite-like phase and Kuzel's salts. For all samples, at the depth of 0–1 mm, the data plot of the Cl/Al ratio becomes flat and runs parallel to the X axis, indicating low chloride binding. This may be attributed to carbonation, as shown in the element mapping (Fig. 11) and TG results (Fig. 18). No obvious trend was observed between the chloride binding capacity and ingress depth, as suggested by some studies [69,70]. The carbonation may lead to a denser structure, and this may contribute to the chloride ingress resistance. This will be explained in detail in the sections that follow.

3.7. Apparent chloride diffusion coefficient

The apparent chloride diffusion coefficients fitted by Fick's second law of the data obtained through EPMA measurements are listed in Table 4. After immersion for 28 days immersion in 0.5 M NaCl, relatively low apparent chloride diffusion coefficients were observed in $NaNO_2$ and $Ca(NO_2)_2$, irrespective of the curing temperature, indicating improved chloride resistance of the samples with added nitrite. Compared to the control group and samples with added Na_2SO_4 cured at 20 °C, the 35-°C-cured specimens showed a more apparent chloride diffusion coefficient, which indicates a higher tendency of chloride penetration. This agrees with the results of chloride binding capacity shown in Fig. 5.

Table 4. Apparent chloride diffusion coefficient and pH

Sample	Apparent chloride diffusion coefficient ($\times 10^{-12}\ m^{-12}/s$)	pH measurement in exposure solution
Con 20 °C	1.0	9.95
Na_2SO_4 20 °C	1.0	10.22
$NaNO_2$ 20 °C	0.65	10.69
$Ca(NO_2)_2$ 20 °C	0.55	10.26
Con 35 °C	1.1	10.28
Na_2SO_4 35 °C	1.1	10.35
$NaNO_2$ 35 °C	0.65	11.22
$Ca(NO_2)_2$ 35 °C	0.65	10.53

4. Discussion

4.1. Impact of additional activators and curing temperature on overall chloride binding content

The impact of additional activators and curing temperatures on the chloride binding capacity of the specimens exposed to 0.5 M NaCl and the effect of pore structure, pH value, phase assemblage, and carbonation are further discussed for a clear understanding of the difference.

As discussed in Section 3.1, although the additional activators and different curing temperatures coarsen the pore structure of the samples, the impact on the reaction degree at a later age was small (Fig. 2). The same amount of C-(A)-S-H was formed, and as shown in Table 5, the average Ca/Si ratio calculated by SEM-EDX was almost the same, indicating similar chloride binding capacities of the samples. As the additional activators mainly changed the type of AFm phase, the impact of AFm phase type and pore structure on the chloride ingress resistance should be discussed further.

As shown in Fig. 10, because different activators were added, SO_4-AFm was mainly formed in samples with added Na_2SO_4, whereas NO_2-AFm, SO_4-AFm, and OH-AFm were mainly formed in samples with added $NaNO_2$ and $Ca(NO_2)_2$. With an increase in the Cl concentration, the hydrotalcite-like phase and AFm phase decomposed to form Cl-AFm. The valence of the anions in the additional activators plays a significant role in the manner in which phase assemblage changes. In the control group, due to the small amount of SO_4^{2-}, Friedel's salts were directly formed, whereas in the samples with additional activators, Kuzel's salts were first formed. Compared to the samples with added $NaNO_2$ and $Ca(NO_2)_2$, evidently, in Na_2SO_4, before chloride exposure, a higher amount of SO_4-AFm formed due to the additional SO_4^{2-} (Fig. 4). After chloride exposure, as the chloride content increased, the ion exchange occurred in the interlayer of the AFm phase, some SO_4^{2-} was replaced by Cl^-, resulting in the formation of the solid solution of SO_4-AFm and Kuzel's. As the chloride ion concentration increases further, the anions in the AFm interlayer are completely replaced by chloride ions, resulting in the formation of Friedel's salts. It should be noted that at low chloride concentration (< 0.2 M), in the control group and the samples added with nitrites, due to less SO_4^{2-} incorporation, the AFm phase transformed to Friedel's salts more rapidly. This is the reason why more Kuzel's salts formed with the Na_2SO_4. According to the composition of Kuzel's salts ($Ca_4Al_2(OH)_{12}Cl(SO_4)_{0.5}(H_2O)_6$) and Friedel's salts ($3CaO{\cdot}Al_2O_3{\cdot}CaCl_2{\cdot}10H_2O$), Kuzel's salts contain less chloride per mol than Friedel's salts. The formation of Kuzel's salts reduced the chloride binding capacity of the samples at a low concentration of NaCl, especially for Na_2SO_4, which can partially explain the low chloride binding capacity of Na_2SO_4, as shown in Fig. 6

In line with previous studies [59,71], an increase in pH was observed when the samples were exposed to a 0.5-M NaCl solution, as shown in Fig. 16. As suggested by Weerdt et al. [59], the change in pH is caused by changes in the phase transformation of the AFm phase (i.e., the formation of AFt from SO_4-AFm or Friedel's salts supplies additional hydroxyl ions). Although thermodynamic modeling predicted that AFt may be formed, as shown in Fig. 8, almost no AFt was formed, and the amount of hemicarboaluminate was relatively stable (Fig. 9). This resulted in the formation of Friedel's salt, which can consume the available aluminum ions that would compete with the formation of AFt, because both reactions require aluminum

ions. In the presence of high concentrations of chloride ions, the Friedel's salt can consume a majority of the available aluminum ions, and thus, they may not contribute the formation of AFt. As shown in Fig. 16, a relatively high pH was observed in the samples that were exposed to NaCl after the chloride equilibrium test, which indicated the occurrence of leaching phenomenon. This phenomenon indicates that a large amount of portlandite was dissolved, which is also supported by the XRD results. A higher pH value was observed in the 35-°C-cured samples, which may be caused by the coarse pore structure (Fig. 3). At higher pH, carbonation occur and the hemicarboaluminate would become more stable. Therefore, the amount of the AFm phase that could be converted to Cl-AFm phase decreased. This could explain the lower total chloride binding capacities of the 35-°C-cured samples, even though more hydration products were formed [25]. Although the measured and predicted trends of pH change are almost consistent, the actual measured pH is lower, and this may be attributed to the dissolution of most portlandite and the formation of large amounts of calcite by natural carbonation, as suggested by the XRD results (Figs. 7 and 8). This also could explain the stability of hemicarboaluminate. However, carbonation may affect the chloride binding capacity because the phase converted to Friedel's salt was reduced, and instead of Friedel's salts, hydrocalumite ($3CaO \cdot Al_2O_3 \cdot 0.5CaCO_3 \cdot 0.5CaCl_2 \cdot 10.8H_2O$) may be formed [72].

Table 5. Average composition of the binder gel phases.

Sample	Si/Ca	Al/Ca	Cl/Si	Mg/Si	Mg/Al
Con 20 °C	0.49	0.24	0.12	0.27	0.51
Na_2SO_4 20 °C	0.42	0.29	0.26	0.30	0.32
$NaNO_2$ 20 °C	0.44	0.21	0.11	0.24	0.48
$Ca(NO_2)_2$ 20 °C	0.42	0.20	0.09	0.26	0.56
Con 35 °C	0.46	0.22	0.12	0.37	0.57
Na_2SO_4 35 °C	0.44	0.29	0.12	0.32	0.31
$NaNO_2$ 35 °C	0.43	0.21	0.09	0.26	0.43
$Ca(NO_2)_2$ 35 °C	0.48	0.25	0.07	0.31	0.57

4.2. Effect of carbonation and leaching on the chloride ingress

The difference in Si/Ca (Fig. 13) and Mg/Al (Fig. 14) between the samples cured at 20 and 35 °C after chloride ingress was not significant. However, for the phase binding chloride, large differences occurred. Fig. 17 further illustrates the changes in the Cl/Al ratios with the changes in the ingress depth. It should be noted that the discussion is simplified, the chloride

binding in C-(A)-S-H was not considered because the chloride binding capacity of C-(A)-S-H is low. Similar to the results shown in Fig. 15, the maximum Cl/Al ratio was observed in samples with added Na_2SO_4 cured at 20 °C. An increase in the Cl/Al ratio from 0-1 to 1-2 mm was observed in all samples, and this may be attributed to carbonation [73]. Another phenomenon is that compared to the specimens cured at 20 °C, the results of the Cl/Al ratio of the specimens cured at 35 °C were much lower, which may be because of heavier carbonation and leaching. A degradation process, referred to as calcium leaching, occurs when calcium ions migrate to the pore solution, and this leads to the gradual dissolution of cement hydrates. The leaching of calcium ions was a common phenomenon in the chloride-rich environment, resulting in the formation of concentration gradients [74]. During the leaching process, calcium hydroxide is the first hydration product that is leached due to its solubility. These findings were confirmed through the TG-DTG analysis results, as shown in Fig. 18. After the chloride diffusion test, four major weight losses were observed in all samples. The weight loss concentrated around 100 °C may be associated with C-(A)-S-H, AFm, and AFt phases [75]. The hump mass loss peaks from 210 to 360 °C were related to hydrotalcite, Friedel's salt, and brucite [32]. The narrow peak around 400 °C was derived from the dehydration of portlandite [43]. The peak associated with carbonates was observed at around 600 °C. After NaCl exposure, the most apparent phenomenon was that as the samples were taken from locations closer to the contact surface, the amount of portlandite decreased, and the corresponding carbonization became more pronounced. The carbonation phenomenon was more severe for the 35-°C-cured samples. Moreover, as shown in Fig. 18, compared to the sample from the center, the closer the sample to the exposure surface, the less the portlandite, although the number of carbonates changed accordingly. Moreover, as shown in Fig. 18, compared to the sample from the center, despite the change in the number of carbonates, the closer the sample to the exposure surface, the lesser the amount of portlandite. The depletion of carbonates due to carbonation results in a decrease in the pH of the concrete. The pH is important because it affects the solubility of portlandite. As the pH decreases, the solubility of portlandite decreases, leading to a reduction in the amount of portlandite that can be formed. Another mechanism that can contribute to the reduction in portlandite during the chloride diffusion test is the leaching of calcium ions. Chloride ions have a high affinity for calcium ions, and as they diffuse through the concrete, they can displace the calcium ions from the portlandite. This may further lead to a decrease in the amount of portlandite available in the samples. However, it is worth noting that not all of the portlandite is converted to carbonate during the chloride diffusion test. In fact, the extent of carbonation depends on several factors, including the concentration of CO_2 in the surrounding environment, the moisture content of the samples, and the duration of exposure. With the leaching of calcium ions, the closer they are to the contact surface, the coarser the pore structure. This is also more conducive to the entry of ions, and it further leads carbonation. The farther they are from the contact surface, the less likely this phenomenon. As a result, not all portlandite are converted into carbonates.

The measured pH value after the chloride diffusion test also supported the leaching phenomenon, and this was consistent with the trend of pH changes in the chloride binding test, the samples cured at higher temperature had higher pH values due to the coarse pore structures. During the diffusion test, a majority of the portlandite dissolved in the pore

solution to form calcite and Ca-rich phases (Fig. 12), which may fill the pore space, and this further led to leaching of calcium that formed the calcite layer at the exposure surface (Fig. 13). The results shown in Table 3 indicate that the changes in the curing temperature do not have a significant impact on the apparent chloride diffusion coefficient, and this may be attributed to the fact that a denser exposure surface has a positive effect on the chloride ingress resistance, especially for samples cured at higher temperatures. This effect has also been reported in a study by Machner et al. of composite cement exposed to NaCl and NaCl + KOH [37]. The dense layer formed on the exposed surface is expected, and some of the filamentous carbonate fills the pores (Figure 12(d)), which also contributes to crack closure [69]. This means that although heavier leaching occurred at a higher curing temperature, the dissolved calcium ions in the pore solution may be carbonated due to the high pH value. The coarse pore structure of the specimens cured at higher temperatures more likely aggravated the leaching phenomenon. Thus, the calcium-rich layer was more likely to precipitate on the exposed surfaces of the samples, and this may have further inhibited the chloride ingress to some extent.

5. Conclusions

The impact of additional activators (Na_2SO_4, $NaNO_2$, and $Ca(NO_2)_2$ and curing temperature (20 and 35 °C) on the chloride ingress resistance upon NaCl exposure of $Ca(OH)_2$-activated GGBFS was studied quantitatively based on a combination of XRD, SEM-EDS,TGA and thermodynamic modeling. The following conclusions were drawn:

- Although Na_2SO_4 and a high curing temperature have a positive impact on the properties of slag activated by $Ca(OH)_2$ at an early stage. However, they make the pore structure coarser and reduces chloride resistance. The resistance to chloride ion attacks exhibits additional-activator dependence.
- Compared to the control group and samples added with nitrites, samples with added Na_2SO_4 showed a lower chloride binding capacity. The difference in the chloride binding capacity at the low chloride concentration was primarily affected by the types of the AFm phase, which further affected the alteration in the phase assemblage after NaCl exposure.
- The chloride binding capacity of the 35-°C-cured samples shows similar trends but a lower chloride binding capacity due to the heavier leaching caused by the coarse pore structures.
- The samples with added nitrites showed higher chloride ingress resistance compared to the control group and samples with added Na_2SO_4, and the impact of the curing temperature was negligible. Although carbonation and leaching have a negative impact on the chloride binding capacity, it seems that the phenomena have a positive effect on the chloride ingress resistance due to the denser layer formed at the exposed surface and carbonates formed in the pore space.

Acknowledgement

This work was supported by "Advanced Research Infrastructure for Materials and Nanotechnology in Japan (ARIM)" of the Ministry of Education, Culture, Sports, Science

and Technology (MEXT). Proposal Number JPMXP1222HK0020.

Author contributions

Qi Zhai: Methodology; Investigation; Writing - original draft. Yibing Zuo: Writing - review & editing; Validation; Software. Kiyofumi Kurumisawa: Conceptualization; Resources; Funding acquisition; Writing - review & editing; Supervision. Aoran Lang: Investigation.

Funding

The Steel Foundation for Environmental Protection Technology and JSPS KAKENHI [grant number 21K04349] and Natural Science Foundation of Hubei province [grant number 2022CFB048] provided funding for this work.

References

[1] H.F.W. Taylor, Cement chemistry, 1997. https://doi.org/10.1680/cc.25929.

[2] IEA (a), CO2 emissions from fuel combustion 2018 overview, OECA/IEA, Paris. (2018).

[3] International Energy Agency (IEA), Statistics report: CO2 Emissions from Fuel Combustion, 2020.

[4] J. Lehne, F. Preston, Making concrete change innovation in low-carbon cement and concrete,The Royal Institute of International Affairs, Chatham House Report Series., (2018) 138. https://www.chathamhouse.org/2018/06/making-concrete-change-innovation-low-carbon-cement-and-concrete.

[5] M. Amran, G. Murali, N.H.A. Khalid, R. Fediuk, T. Ozbakkaloglu, Y.H. Lee, S. Haruna, Y.Y. Lee, Slag uses in making an ecofriendly and sustainable concrete: A review, Constr. Build. Mater. 272 (2021) 121942. https://doi.org/10.1016/j.conbuildmat.2020.121942.

[6] S.F.A. Shah, B. Chen, S.Y. Oderji, M.A. Haque, M.R. Ahmad, Improvement of early strength of fly ash-slag based one-part alkali activated mortar, Constr. Build. Mater. 246 (2020). https://doi.org/10.1016/j.conbuildmat.2020.118533.

[7] J.L. Provis, Alkali-activated materials, Cem. Concr. Res. 114 (2018). https://doi.org/10.1016/j.cemconres.2017.02.009.

[8] H. Yu, Y. Yi, C. Unluer, Heat of hydration, bleeding, viscosity, setting of Ca(OH)2-GGBS and MgO-GGBS grouts, Constr. Build. Mater. 270 (2021) 121839. https://doi.org/10.1016/j.conbuildmat.2020.121839.

[9] C. Shi, A.F. Jiménez, A. Palomo, New cements for the 21st century: The pursuit of an alternative to Portland cement, Cem. Concr. Res. 41 (2011). https://doi.org/10.1016/j.cemconres.2011.03.016.

[10] V. Vishwakarma, D. Ramachandran, Green Concrete mix using solid waste and nanoparticles as alternatives – A review, Constr. Build. Mater. 162 (2018) 96–103. https://doi.org/10.1016/j.conbuildmat.2017.11.174.

[11] D.W. Law, A.A. Adam, T.K. Molyneaux, I. Patnaikuni, Durability assessment of alkali activated slag (AAS) concrete, Mater. Struct. Constr. 45 (2012). https://doi.org/10.1617/s11527-012-9842-1.

[12] J. Osio-Norgaard, J.P. Gevaudan, W. V. Srubar, A review of chloride transport in alkali-activated cement paste, mortar, and concrete, Constr. Build. Mater. 186 (2018) 191–206. https://doi.org/10.1016/j.conbuildmat.2018.07.119.

[13] M. Torres-Carrasco, C. Rodríguez-Puertas, M. Del Mar Alonso, F. Puertas, Alkali activated slag cements using waste glass as alternative activators. Rheological behaviour, Bol. La Soc. Esp. Ceram. y Vidr. 54 (2015). https://doi.org/10.1016/j.bsecv.2015.03.004.

[14] A. Fernández-Jiménez, F. Puertas, Setting of alkali-activated slag cement. Influence of activator nature, Adv. Cem. Res. 13 (2001). https://doi.org/10.1680/adcr.2001.13.3.115.

[15] Z. Chen, H. Ye, Influence of metakaolin and limestone on chloride binding of slag activated by mixed magnesium oxide and sodium hydroxide, Cem. Concr. Compos. 127 (2022) 104397. https://doi.org/10.1016/j.cemconcomp.2021.104397.

[16] H. Ye, L. Huang, Z. Chen, Influence of activator composition on the chloride binding capacity of alkali-activated slag, Cem. Concr. Compos. 104 (2019) 103368. https://doi.org/10.1016/j.cemconcomp.2019.103368.

[17] J. Zhang, C. Shi, Z. Zhang, Chloride binding of alkali-activated slag/fly ash cements, Constr. Build. Mater. 226 (2019) 21–31. https://doi.org/10.1016/j.conbuildmat.2019.07.281.

[18] C. Shi, R.L. Day, A calorimetric study of early hydration of alkali-slag cements, Cem. Concr. Res. 25 (1995). https://doi.org/10.1016/0008-8846(95)00126-W.

[19] K.H. Yang, K.H. Lee, J.K. Song, M.H. Gong, Properties and sustainability of alkali-activated slag foamed concrete, J. Clean. Prod. 68 (2014). https://doi.org/10.1016/j.jclepro.2013.12.068.

[20] M. Palacios, S. Gismera, M.M. Alonso, J.B. d'Espinose de Lacaillerie, B. Lothenbach, A. Favier, C. Brumaud, F. Puertas, Early reactivity of sodium silicate-activated slag pastes and its impact on rheological properties, Cem. Concr. Res. 140 (2021). https://doi.org/10.1016/j.cemconres.2020.106302.

[21] Y. Jeong, J.E. Oh, Y. Jun, J. Park, J.H. Ha, S.G. Sohn, Influence of four additional activators on hydrated-lime [Ca(OH)2] activated ground granulated blast-furnace slag, Cem. Concr. Compos. 65 (2016) 1–10. https://doi.org/10.1016/j.cemconcomp.2015.10.007.

[22] A. Fernández-Jiménez, F. Puertas, I. Sobrados, J. Sanz, Structure of calcium silicate hydrates formed in alkaline-activated slag: Influence of the type of alkaline activator, J. Am. Ceram. Soc. 86 (2003). https://doi.org/10.1111/j.1151-2916.2003.tb03481.x.

[23] Q. Zhai, K. Kurumisawa, Effect of accelerators on Ca(OH)2 activated ground granulated blast-furnace slag at low curing temperature, Cem. Concr. Compos. 124 (2021) 104272. https://doi.org/10.1016/j.cemconcomp.2021.104272.

[24] R. Snellings, A. Machner, G. Bolte, H. Kamyab, P. Durdzinski, P. Teck, M. Zajac, A. Muller, K. de Weerdt, M. Ben Haha, Hydration kinetics of ternary slag-limestone cements: Impact of

water to binder ratio and curing temperature, Cem. Concr. Res. 151 (2022). https://doi.org/10.1016/j.cemconres.2021.106647.

[25] F. Avet, K. Scrivener, Influence of pH on the chloride binding capacity of Limestone Calcined Clay Cements (LC3), Cem. Concr. Res. 131 (2020) 106031. https://doi.org/10.1016/j.cemconres.2020.106031.

[26] J.S.J. van Deventer, J.L. Provis, P. Duxson, G.C. Lukey, Reaction mechanisms in the geopolymeric conversion of inorganic waste to useful products, J. Hazard. Mater. 139 (2007). https://doi.org/10.1016/j.jhazmat.2006.02.044.

[27] H. Xu, J.S.J. Van Deventer, The geopolymerisation of alumino-silicate minerals, Int. J. Miner. Process. 59 (2000). https://doi.org/10.1016/S0301-7516(99)00074-5.

[28] S. Park, H.M. Park, H.N. Yoon, J. Seo, C.M. Yang, J.L. Provis, B. Yang, Hydration kinetics and products of MgO-activated blast furnace slag, Constr. Build. Mater. 249 (2020). https://doi.org/10.1016/j.conbuildmat.2020.118700.

[29] H. Ye, L. Huang, Z. Chen, Influence of activator composition on the chloride binding capacity of alkali-activated slag, Cem. Concr. Compos. 104 (2019) 103368. https://doi.org/10.1016/j.cemconcomp.2019.103368.

[30] O. Kayali, M.S.H. Khan, M. Sharfuddin Ahmed, The role of hydrotalcite in chloride binding and corrosion protection in concretes with ground granulated blast furnace slag, Cem. Concr. Compos. 34 (2012) 936–945. https://doi.org/10.1016/j.cemconcomp.2012.04.009.

[31] X. Ke, S.A. Bernal, J.L. Provis, Uptake of chloride and carbonate by Mg-Al and Ca-Al layered double hydroxides in simulated pore solutions of alkali-activated slag cement, Cem. Concr. Res. 100 (2017) 1–13. https://doi.org/10.1016/j.cemconres.2017.05.015.

[32] Z. Chen, H. Ye, Sequestration and release of nitrite and nitrate in alkali-activated slag: A route toward smart corrosion control, Cem. Concr. Res. 143 (2021) 106398. https://doi.org/10.1016/j.cemconres.2021.106398.

[33] S. Miyata, Anion-exchange properties of hydrotalcite-like compounds., Clays Clay Miner. 31 (1983). https://doi.org/10.1346/CCMN.1983.0310409.

[34] U.. Birnin-Yauri, F.. Glasser, Friedel's salt, Ca2Al(OH)6(Cl,OH)·2H2O: its solid solutions and their role in chloride binding, Cem. Concr. Res. 28 (1998) 1713–1723. https://doi.org/10.1016/S0008-8846(98)00162-8.

[35] M.S.H. Khan, O. Kayali, Chloride binding ability and the onset corrosion threat on alkali-activated GGBFS and binary blend pastes, Eur. J. Environ. Civ. Eng. 22 (2018) 1023–1039. https://doi.org/10.1080/19648189.2016.1230522.

[36] M. Balonis, B. Lothenbach, G. Le Saout, F.P. Glasser, Impact of chloride on the mineralogy of hydrated Portland cement systems, Cem. Concr. Res. 40 (2010). https://doi.org/10.1016/j.cemconres.2010.03.002.

[37] A. Machner, M.H. Bjørndal, H. Justnes, L. Hanžič, A. Šajna, Y. Gu, B. Bary, M. Ben Haha, M.R. Geiker, K. De Weerdt, Effect of leaching on the composition of hydration phases during

chloride exposure of mortar, Cem. Concr. Res. 153 (2022) 106691. https://doi.org/10.1016/j.cemconres.2021.106691.

[38] J. Tritthart, Chloride binding in cement II. The influence of the hydroxide concentration in the pore solution of hardened cement paste on chloride binding, Cem. Concr. Res. 19 (1989). https://doi.org/10.1016/0008-8846(89)90039-2.

[39] G. Plusquellec, A. Nonat, Interactions between calcium silicate hydrate (C-S-H) and calcium chloride, bromide and nitrate, Cem. Concr. Res. 90 (2016) 89–96. https://doi.org/10.1016/j.cemconres.2016.08.002.

[40] C. Arya, N.R. Buenfeld, J.B. Newman, Factors influencing chloride-binding in concrete, Cem. Concr. Res. 20 (1990) 291–300. https://doi.org/10.1016/0008-8846(90)90083-A.

[41] G. Kovalchuk, A. Fernández-Jiménez, A. Palomo, Alkali-activated fly ash: Effect of thermal curing conditions on mechanical and microstructural development - Part II, Fuel. 86 (2007). https://doi.org/10.1016/j.fuel.2006.07.010.

[42] D. Bondar, C.J. Lynsdale, N.B. Milestone, N. Hassani, Oxygen and chloride permeability of alkali-activated natural pozzolan concrete, ACI Mater. J. 109 (2012). https://doi.org/10.14359/51683570.

[43] O.R. Ogirigbo, L. Black, Chloride binding and diffusion in slag blends: Influence of slag composition and temperature, Constr. Build. Mater. 149 (2017) 816–825. https://doi.org/10.1016/j.conbuildmat.2017.05.184.

[44] P. Li, J. Tang, Y. Bai, X. Chen, J. Chen, Experimental study on the pH for activating ground granulated blast-furnace slag activity at different temperatures, Sadhana - Acad. Proc. Eng. Sci. 44 (2019). https://doi.org/10.1007/s12046-019-1204-z.

[45] S.D. Wang, K.L. Scrivener, P.L. Pratt, Factors affecting the strength of alkali-activated slag, Cem. Concr. Res. 24 (1994). https://doi.org/10.1016/0008-8846(94)90026-4.

[46] A. Fernández-Jiménez, J.G. Palomo, F. Puertas, Alkali-activated slag mortars: Mechanical strength behaviour, Cem. Concr. Res. 29 (1999). https://doi.org/10.1016/S0008-8846(99)00154-4.

[47] G. Jing, Z. Ye, J. Wu, S. Wang, X. Cheng, V. Strokova, V. Nelyubova, Introducing reduced graphene oxide to enhance the thermal properties of cement composites, Cem. Concr. Compos. 109 (2020). https://doi.org/10.1016/j.cemconcomp.2020.103559.

[48] Q. Zhai, K. Kurumisawa, Mechanisms of inorganic salts on Ca(OH)2-activated ground granulated blast-furnace slag curing under different temperatures, Constr. Build. Mater. 338 (2022). https://doi.org/10.1016/j.conbuildmat.2022.127637.

[49] P.T. Durdziński, M. Ben Haha, S.A. Bernal, N. De Belie, E. Gruyaert, B. Lothenbach, E. Menéndez Méndez, J.L. Provis, A. Schöler, C. Stabler, Z. Tan, Y. Villagrán Zaccardi, A. Vollpracht, F. Winnefeld, M. Zając, K.L. Scrivener, Outcomes of the RILEM round robin on degree of reaction of slag and fly ash in blended cements, Mater. Struct. Constr. 50 (2017). https://doi.org/10.1617/s11527-017-1002-1.

[50] T. Luping, L.-O. Nilsson, Chloride binding capacity and binding isotherms of OPC pastes and mortars, Cem. Concr. Res. 23 (1993) 247–253. https://doi.org/10.1016/0008-8846(93)90089-R.

[51] N. Doebelin, R. Kleeberg, Profex: A graphical user interface for the Rietveld refinement program BGMN, J. Appl. Crystallogr. 48 (2015). https://doi.org/10.1107/S1600576715014685.

[52] M. Collepardi, A. Marcialis, R. Turriziani, Penetration of Chloride Ions into Cement Pastes and Concretes, J. Am. Ceram. Soc. 55 (1972). https://doi.org/10.1111/j.1151-2916.1972.tb13424.x.

[53] Y. Zuo, Effect of chloride salt on the phase evolution in alkali-activated slag cements through thermodynamic modelling, Appl. Geochemistry. 136 (2022) 105169. https://doi.org/10.1016/j.apgeochem.2021.105169.

[54] H.M. Jennings, A. Kumar, G. Sant, Quantitative discrimination of the nano-pore-structure of cement paste during drying: New insights from water sorption isotherms, Cem. Concr. Res. 76 (2015). https://doi.org/10.1016/j.cemconres.2015.05.006.

[55] R.J. Myers, S.A. Bernal, J.L. Provis, Phase diagrams for alkali-activated slag binders, Cem. Concr. Res. 95 (2017) 30–38. https://doi.org/10.1016/j.cemconres.2017.02.006.

[56] M. Balonis, The Influence of Inorganic Chemical Accelerators and Corrosion Inhibitors on the Mineralogy of Hydrated Portland Cement Systems, 2010.

[57] M.D.A. Thomas, R.D. Hooton, A. Scott, H. Zibara, The effect of supplementary cementitious materials on chloride binding in hardened cement paste, Cem. Concr. Res. 42 (2012). https://doi.org/10.1016/j.cemconres.2011.01.001.

[58] A. Ipavec, T. Vuk, R. Gabrovšek, V. Kaučič, Chloride binding into hydrated blended cements: The influence of limestone and alkalinity, Cem. Concr. Res. 48 (2013). https://doi.org/10.1016/j.cemconres.2013.02.010.

[59] K. De Weerdt, A. Colombo, L. Coppola, H. Justnes, M.R. Geiker, Impact of the associated cation on chloride binding of Portland cement paste, Cem. Concr. Res. 68 (2015) 196–202. https://doi.org/10.1016/j.cemconres.2014.01.027.

[60] C. Fu, H. Ye, K. Zhu, D. Fang, J. Zhou, Alkali cation effects on chloride binding of alkali-activated fly ash and metakaolin geopolymers, Cem. Concr. Compos. 114 (2020) 103721. https://doi.org/10.1016/j.cemconcomp.2020.103721.

[61] F. Georget, B. Lothenbach, W. Wilson, F. Zunino, K.L. Scrivener, Stability of hemicarbonate under cement paste-like conditions, Cem. Concr. Res. 153 (2022). https://doi.org/10.1016/j.cemconres.2021.106692.

[62] J. Zuo, B. Wu, C. Luo, B. Dong, F. Xing, Preparation of MgAl layered double hydroxides intercalated with nitrite ions and corrosion protection of steel bars in simulated carbonated concrete pore solution, Corros. Sci. 152 (2019) 120–129. https://doi.org/10.1016/j.corsci.2019.03.007.

[63] Y. Cao, L. Guo, B. Chen, J. Wu, Thermodynamic modelling and experimental investigation on chloride binding in cement exposed to chloride and chloride-sulfate solution, Constr. Build. Mater. 246 (2020) 118398. https://doi.org/10.1016/j.conbuildmat.2020.118398.

[64] A. Mesbah, C. Cau-Dit-Coumes, G. Renaudin, F. Frizon, F. Leroux, Uptake of chloride and carbonate ions by calcium monosulfoaluminate hydrate, Cem. Concr. Res. 42 (2012). https://doi.org/10.1016/j.cemconres.2012.05.012.

[65] B. Li, Q. Li, W. Chen, Spatial zonation of a hydrotalcite-like phase in the inner product of slag: New insights into the hydration mechanism, Cem. Concr. Res. 145 (2021). https://doi.org/10.1016/j.cemconres.2021.106460.

[66] M. Chabannes, H. Kazemi-kamyab, J. Trigallez, R. Snellings, Cement and Concrete Research Performance and microstructure development of lime – calcined fluvial sediment binders under different curing conditions, Cem. Concr. Res. 160 (2022) 106903. https://doi.org/10.1016/j.cemconres.2022.106903.

[67] S.J. Mills, A.G. Christy, J.-M.R. Génin, T. Kameda, F. Colombo, Nomenclature of the hydrotalcite supergroup: natural layered double hydroxides, Mineral. Mag. 76 (2012). https://doi.org/10.1180/minmag.2012.076.5.10.

[68] E. L'Hôpital, B. Lothenbach, G. Le Saout, D. Kulik, K. Scrivener, Incorporation of aluminium in calcium-silicate-hydrates, Cem. Concr. Res. 75 (2015). https://doi.org/10.1016/j.cemconres.2015.04.007.

[69] X. Wu, H. Huang, H. Liu, J. Hu, J. Wei, Z. Jiang, G. Ye, Q. Yu, B. Lothenbach, Reactions of self-healing agents and the chemical binding of aggressive ions in sea water: Thermodynamics and kinetics, Cem. Concr. Res. 145 (2021). https://doi.org/10.1016/j.cemconres.2021.106450.

[70] M. Maes, N. De Belie, Influence of chlorides on magnesium sulphate attack for mortars with Portland cement and slag based binders, Constr. Build. Mater. 155 (2017) 630–642. https://doi.org/10.1016/j.conbuildmat.2017.07.201.

[71] K. De Weerdt, D. Orsáková, M.R. Geiker, The impact of sulphate and magnesium on chloride binding in Portland cement paste, Cem. Concr. Res. 65 (2014) 30–40. https://doi.org/10.1016/j.cemconres.2014.07.007.

[72] A. Mesbah, J.P. Rapin, M. Franąois, C. Cau-Dit-Coumes, F. Frizon, F. Leroux, G. Renaudin, Crystal structures and phase transition of cementitious Bi-anionic AFm-(Cl-, CO32-) compounds, J. Am. Ceram. Soc. 94 (2011). https://doi.org/10.1111/j.1551-2916.2010.04050.x.

[73] P. Hemstad, A. Machner, K. De Weerdt, The effect of artificial leaching with HCl on chloride binding in ordinary Portland cement paste, Cem. Concr. Res. 130 (2020) 105976. https://doi.org/10.1016/j.cemconres.2020.105976.

[74] Y.S. Choi, E.I. Yang, Effect of calcium leaching on the pore structure, strength, and chloride penetration resistance in concrete specimens, Nuclear Engineering and Design. 259 (2013). https://doi.org/10.1016/j.nucengdes.2013.02.049.

[75] Z. Shi, M.R. Geiker, B. Lothenbach, K. De Weerdt, S.F. Garzón, K. Enemark-Rasmussen, J. Skibsted, Friedel's salt profiles from thermogravimetric analysis and thermodynamic modelling of Portland cement-based mortars exposed to sodium chloride solution, Cem. Concr.

Compos. 78 (2017). https://doi.org/10.1016/j.cemconcomp.2017.01.002.

Figure Captions

Fig. 1. Compressive strength of mortars.

Fig. 2. Reaction degree of pastes at 3, 7, and 28 days.

Fig. 3. Pore structure of $Ca(OH)_2$-activated GGBFS pastes at 28 days. (a) Pore size distribution at 20 °C; (b) Cumulative pore volume at 20 °C; (c) Pore size distribution at 35 °C; (d) Cumulative pore volume at 35 °C.

Fig. 4. XRD patterns of pastes at 28 days. AFt: Ettringite, Ms: Monosulfoaluminate, Hc: Hemicaroaluminate, CH: Portlandite, CC: Calcite.

Fig. 5. Chloride binding isotherms for pastes with additional activators cured at 20 and 35 °C and chloride binding capacity of various binders reported in Refs.[17,50,59,60,75,76].

Fig. 6. Total chloride binding data fitted by the Langmuir and Freundlich isotherms.

Fig. 7. XRD patterns of pastes cured at 20 °C after chloride exposure. (a) Pastes after exposure to the specified chloride concentrations. (b) Enlarged XRD patterns between 7 to 16° of pastes before exposure and after exposure to 0.025 and 0.5 M chloride.

Fig. 8. XRD patterns of pastes cured at 35 °C after chloride exposure. (a) Pastes after exposure to specified chloride concentrations. (b) Enlarged XRD patterns between 7 to 16° of pastes before exposure and after exposure to 0.025 and 0.5 M chloride.

Fig. 9. Quantified key phases determined by XRD-Rietveld analysis.

Fig. 10. Phase assemblage of samples cured at 20 °C as function of chloride concentration. (a) control group, (b) Na_2SO_4, (c) $Ca(NO_2)_2$, (d) $NaNO_2$.

Fig. 11. Element map of samples cured at 35 °C after NaCl exposure. Exposed surface is located at right of the image.

Fig. 12. Microstructure analysis of samples cured at 35 °C by BSE-EDX. (a) Control samples before chloride exposure, (b) Control samples after chloride exposure, (c) Na_2SO_4, (d) $NaNO_2$ and (e) $Ca(NO_2)_2$. △: Kuzel's salt, □: Portlandite.

Fig. 13. Al/Ca versus Si/Ca atomic ratios after samples were exposed to NaCl solutions at depths from 0 to 7 mm obtained by SEM-EDX. (a) 20 and (b) 35 °C. std: analyzed point from the center layer of samples.

Fig. 14. Mg/Si versus Al/Si atomic ratios after the samples were exposed to NaCl solutions at depths from 0 to 7 mm obtained by SEM-EDX. (a) 20 and (b) 35 °C. std: powder extracted from center layer of the samples.

Fig. 15. Al/Ca versus Cl/Ca atomic ratios after samples were exposed to NaCl solutions at depths from 0 to 7 mm obtained by SEM-EDX. (a) 20 and (b) 35 °C. std: powder extracted from center layer of the samples.

Fig. 16. Comparison between measured and predicted pH as a function of NaCl concentration.

Fig. 17. Comparison of Cl/Al ratios as a function of ingress depth of the samples exposed to NaCl solution.

Fig. 18. Comparison of TG and DTG curves of samples after exposure to 0.5 M NaCl for selected grinding layers. (a) control group, (b) Na_2SO_4, (c) $NaNO_2$ and (d) $Ca(NO_2)_2$. Fs: Friedel's salt.

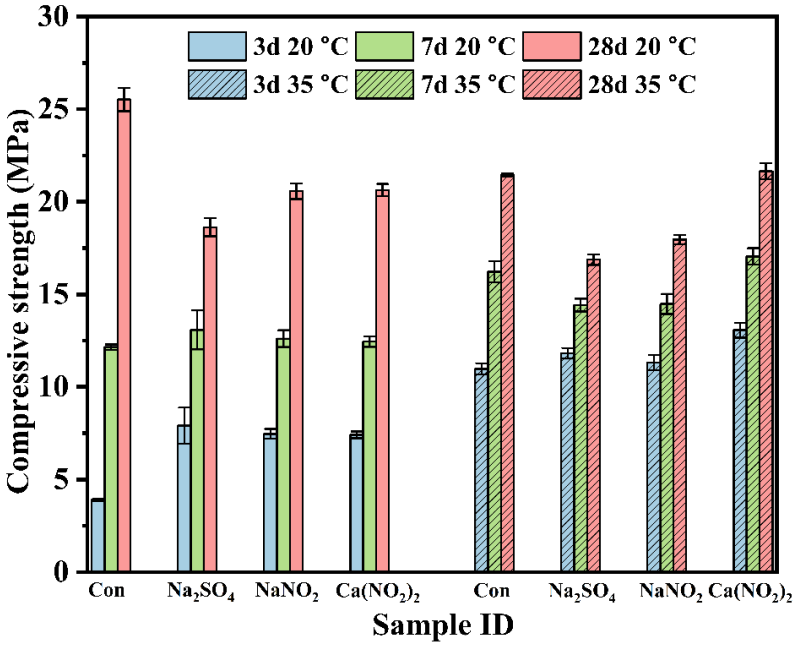
30
25
20
15
10
5
0
Compressive strength (MPa)
3d 20 °C
7d 20 °C
28d 20 °C
3d 35 °C
7d 35 °C
28d 35 °C
Con
Na2SO4
NaNO2
Ca(NO2)2
Con
Na2SO4
NaNO2
Ca(NO2)2
Sample ID

Fig. 1.

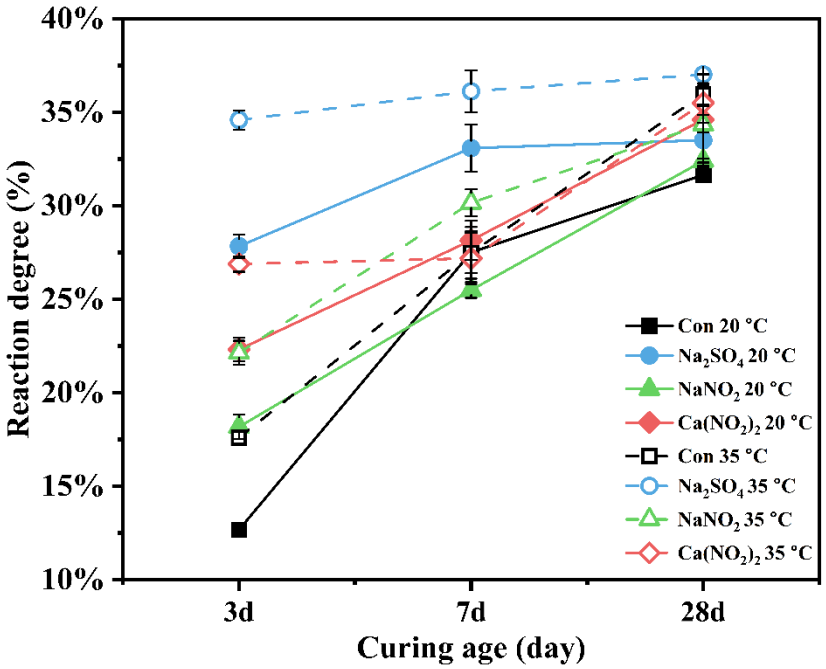
40%
35%
30%
25%
20%
15%
10%
Reaction degree (%)
3d
7d
28d
Curing age (day)
Con 20 °C
Na2SO4 20 °C
NaNO2 20 °C
Ca(NO2)2 20 °C
Con 35 °C
Na2SO4 35 °C
NaNO2 35 °C
Ca(NO2)2 35 °C

Fig. 2.

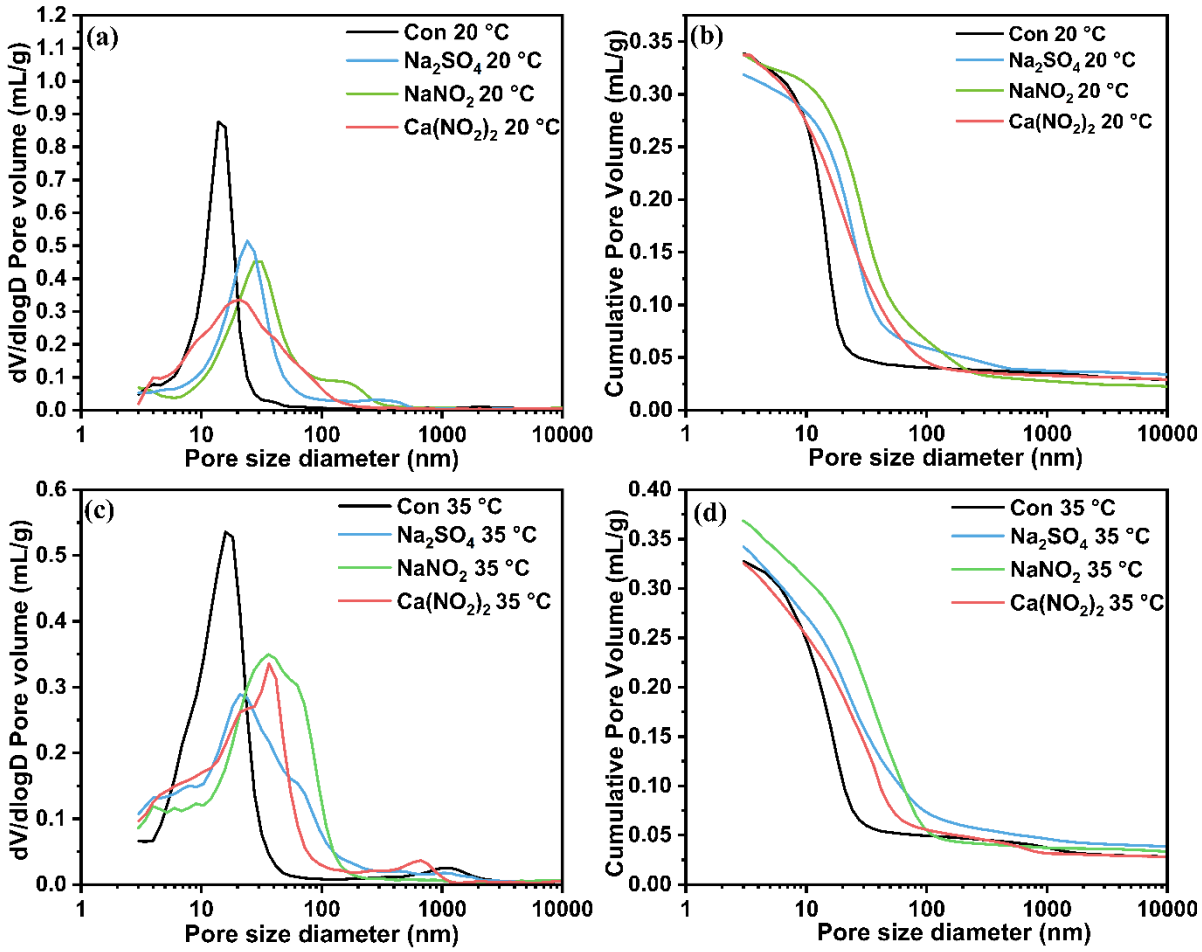
(a)
Con 20 °C
Na2SO4 20 °C
NaNO2 20 °C
Ca(NO2)2 20 °C
dV/dlogD Pore volume (mL/g)
Pore size diameter (nm)
(b)
Cumulative Pore Volume (mL/g)
(c)
Con 35 °C
Na2SO4 35 °C
NaNO2 35 °C
Ca(NO2)2 35 °C
(d)

Fig. 3.

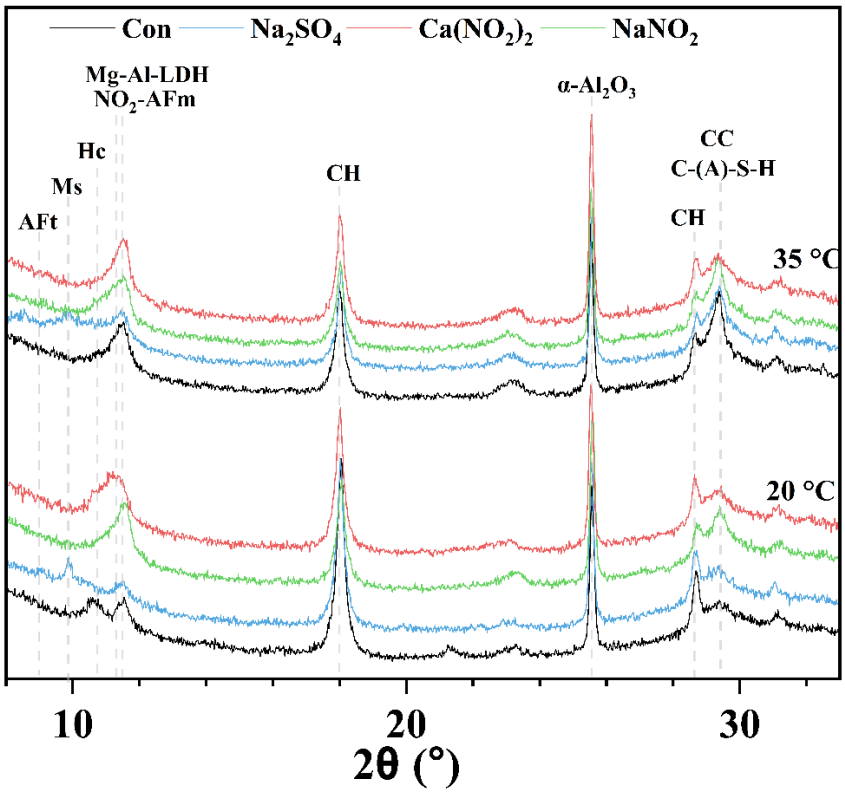
Con
Na2SO4
Ca(NO2)2
NaNO2
Mg-Al-LDH
NO2-AFm
α-Al2O3
Hc
Ms
AFt
CH
CC
C-(A)-S-H
CH
35 °C
20 °C
10
20
30
2θ (°)

Fig. 4.

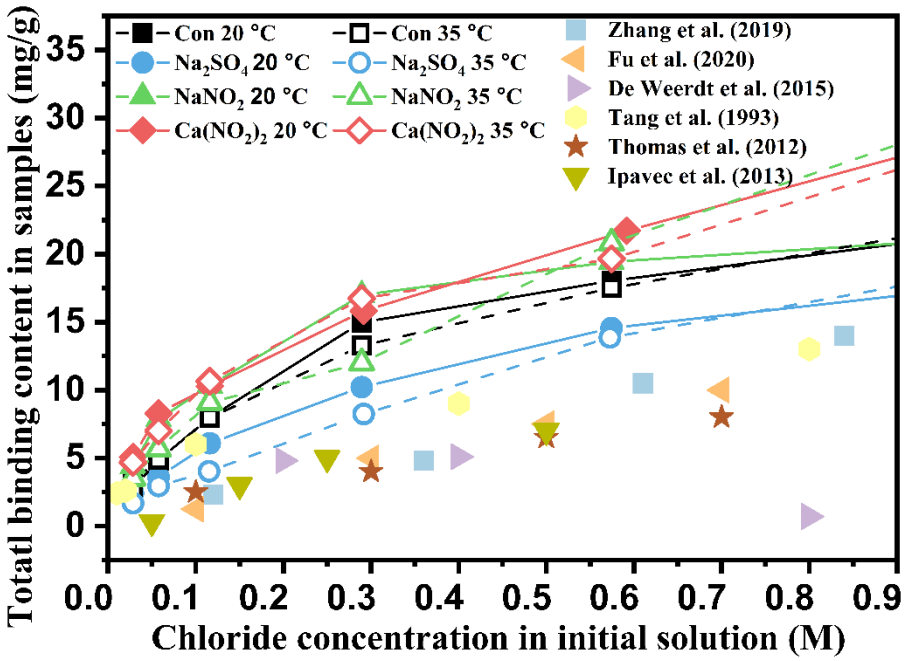
Con 20 °C
Con 35 °C
Na2SO4 20 °C
Na2SO4 35 °C
NaNO2 20 °C
NaNO2 35 °C
Ca(NO2)2 20 °C
Ca(NO2)2 35 °C
Zhang et al. (2019)
Fu et al. (2020)
De Weerdt et al. (2015)
Tang et al. (1993)
Thomas et al. (2012)
Ipavec et al. (2013)
Totatl binding content in samples (mg/g)
Chloride concentration in initial solution (M)
0
5
10
15
20
25
30
35
0.0
0.1
0.2
0.3
0.4
0.5
0.6
0.7
0.8
0.9

Fig. 5.

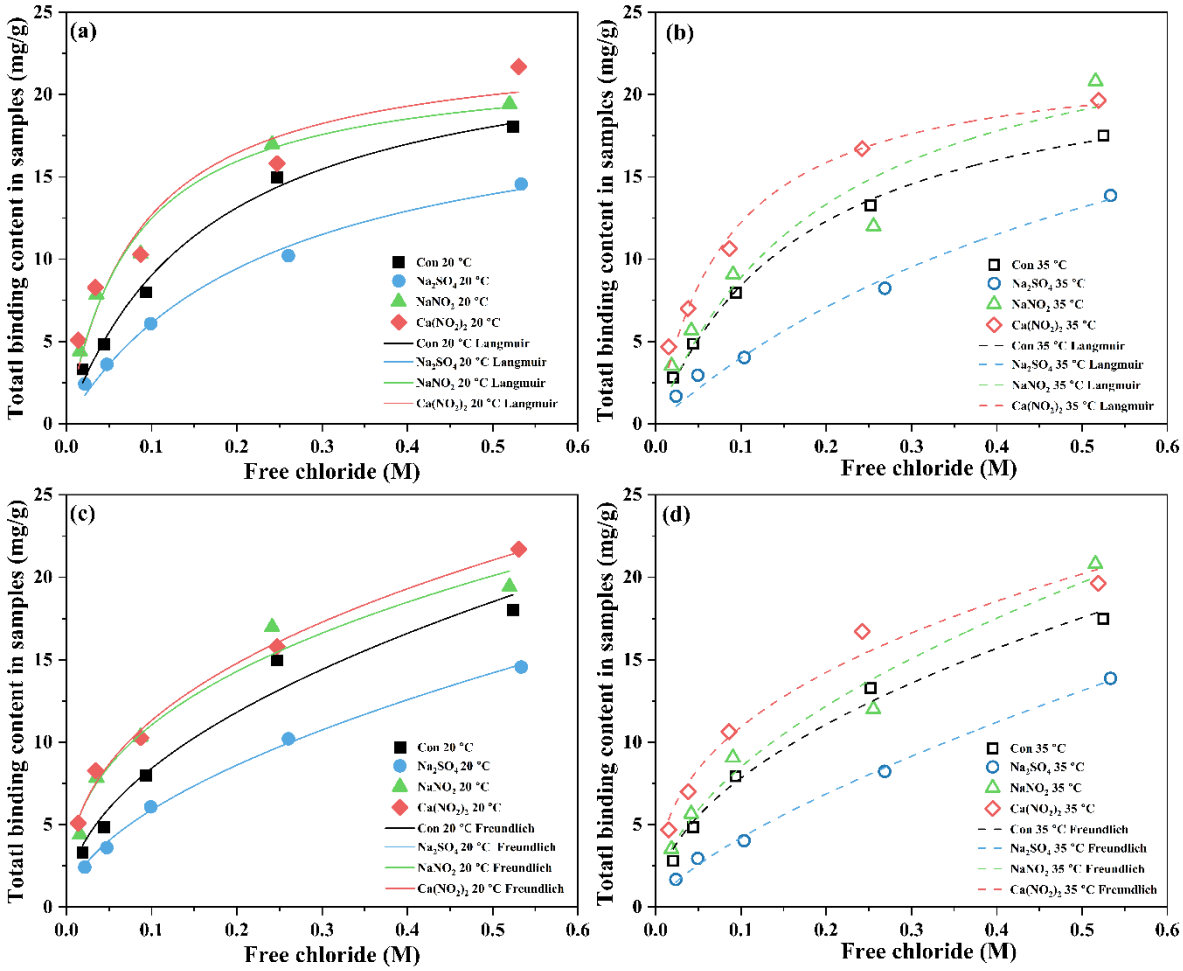
(a)
(b)
(c)
(d)
Totatl binding content in samples (mg/g)
Free chloride (M)
Con 20 °C
Na2SO4 20 °C
NaNO2 20 °C
Ca(NO2)2 20 °C
Con 20 °C Langmuir
Na2SO4 20 °C Langmuir
NaNO2 20 °C Langmuir
Ca(NO3)2 20 °C Langmuir
Con 35 °C
Na2SO4 35 °C
NaNO2 35 °C
Ca(NO2)2 35 °C
Con 35 °C Langmuir
Na2SO4 35 °C Langmuir
NaNO2 35 °C Langmuir
Ca(NO3)2 35 °C Langmuir
Con 20 °C Freundlich
Na2SO4 20 °C Freundlich
NaNO2 20 °C Freundlich
Ca(NO2)2 20 °C Freundlich
Con 35 °C Freundlich
Na2SO4 35 °C Freundlich
NaNO2 35 °C Freundlich
Ca(NO2)2 35 °C Freundlich

Fig. 6.

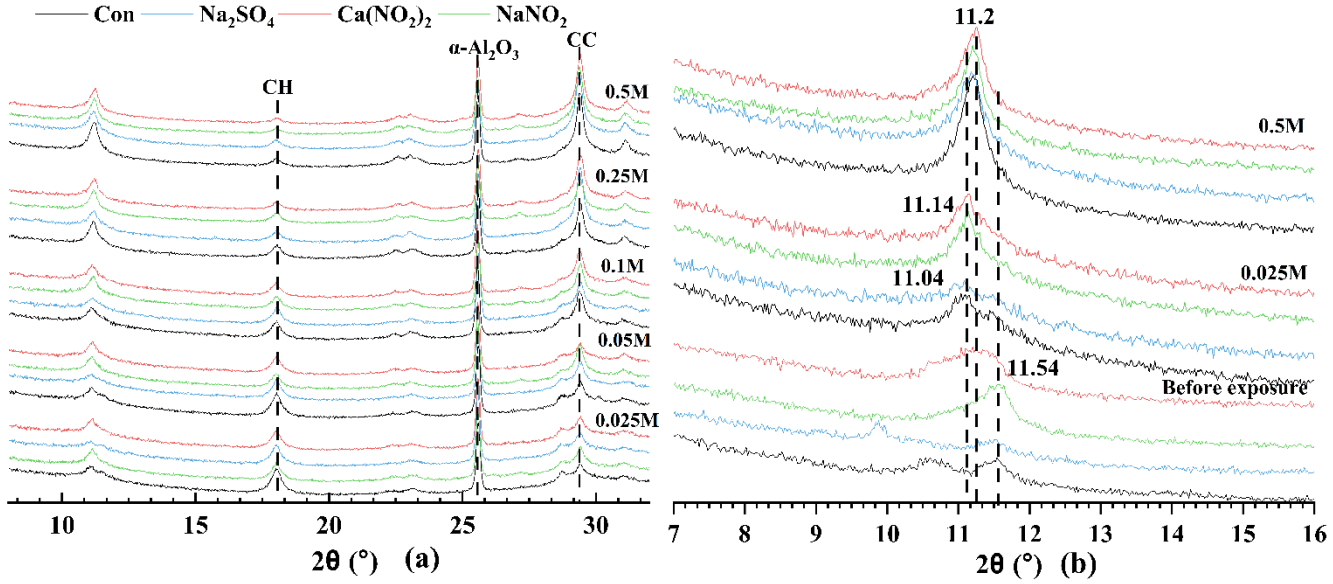
Con
Na2SO4
Ca(NO2)2
NaNO2
α-Al2O3
CC
CH
0.5M
0.25M
0.1M
0.05M
0.025M
10
15
20
25
30
2θ (°) (a)
11.2
11.14
11.04
11.54
0.5M
0.025M
Before exposure
7
8
9
10
11
12
13
14
15
16
2θ (°) (b)

Fig. 7.

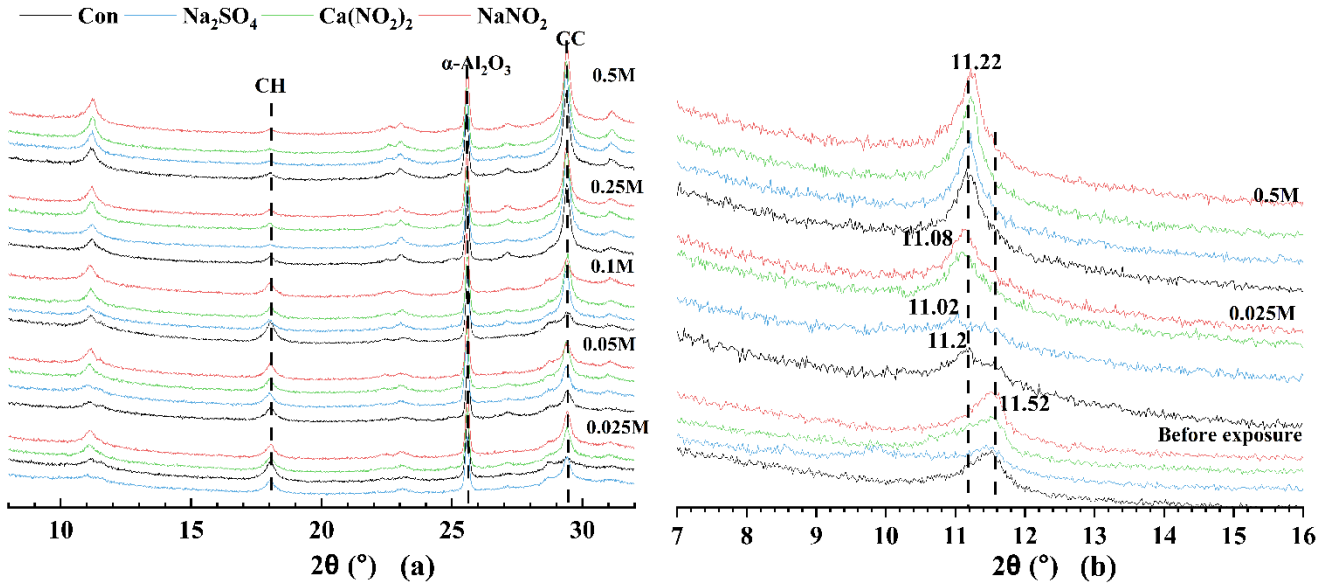
Con
Na2SO4
Ca(NO2)2
NaNO2
CH
α-Al2O3
GC
0.5M
0.25M
0.1M
0.05M
0.025M
10
15
20
25
30
2θ (°) (a)
11.22
11.08
11.02
11.2
11.52
0.5M
0.025M
Before exposure
7
8
9
10
11
12
13
14
15
16
2θ (°) (b)

Fig. 8.

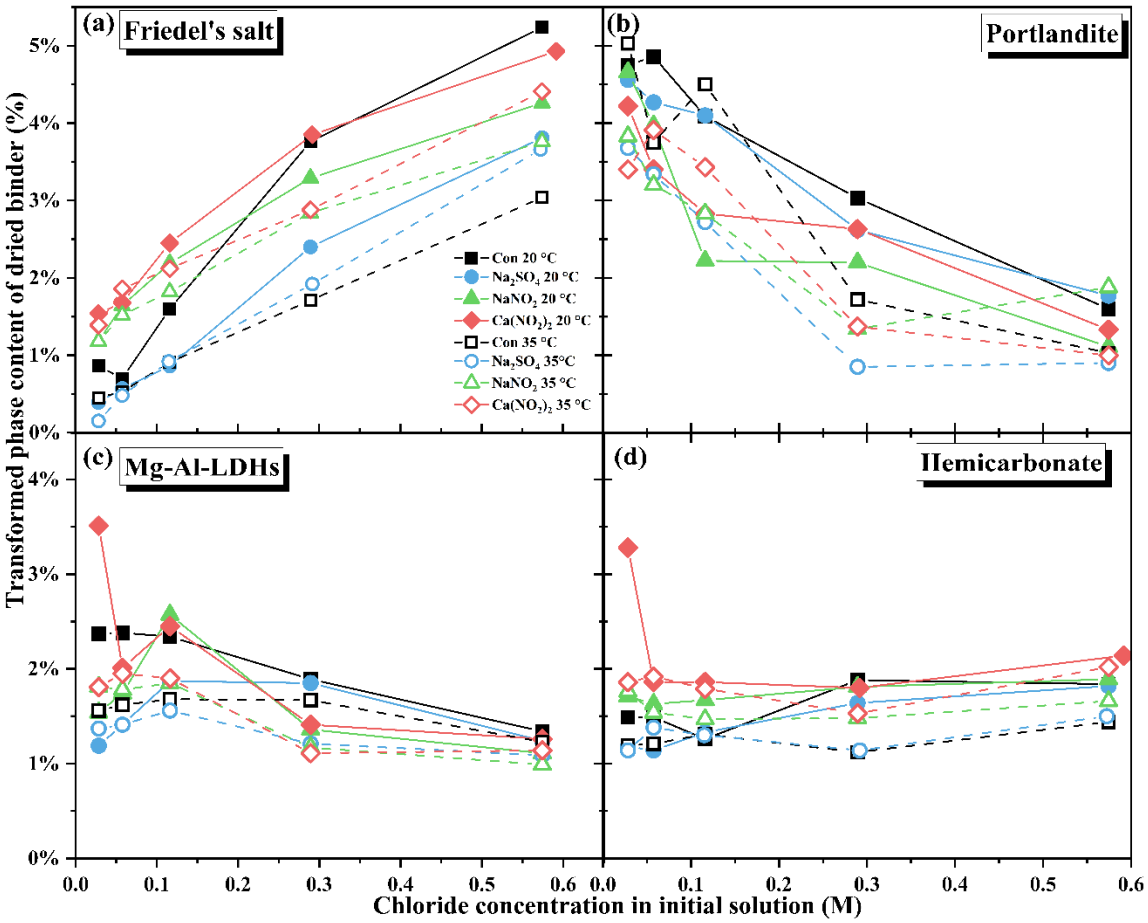
(a) Friedel's salt
(b) Portlandite
(c) Mg-Al-LDHs
(d) Hemicarbonate
Con 20 °C
Na2SO4 20 °C
NaNO2 20 °C
Ca(NO2)2 20 °C
Con 35 °C
Na2SO4 35°C
NaNO2 35 °C
Ca(NO2)2 35 °C
Transformed phase content of dried binder (%)
Chloride concentration in initial solution (M)
0%
1%
2%
3%
4%
5%
0.0
0.1
0.2
0.3
0.4
0.5
0.6

Fig. 9.

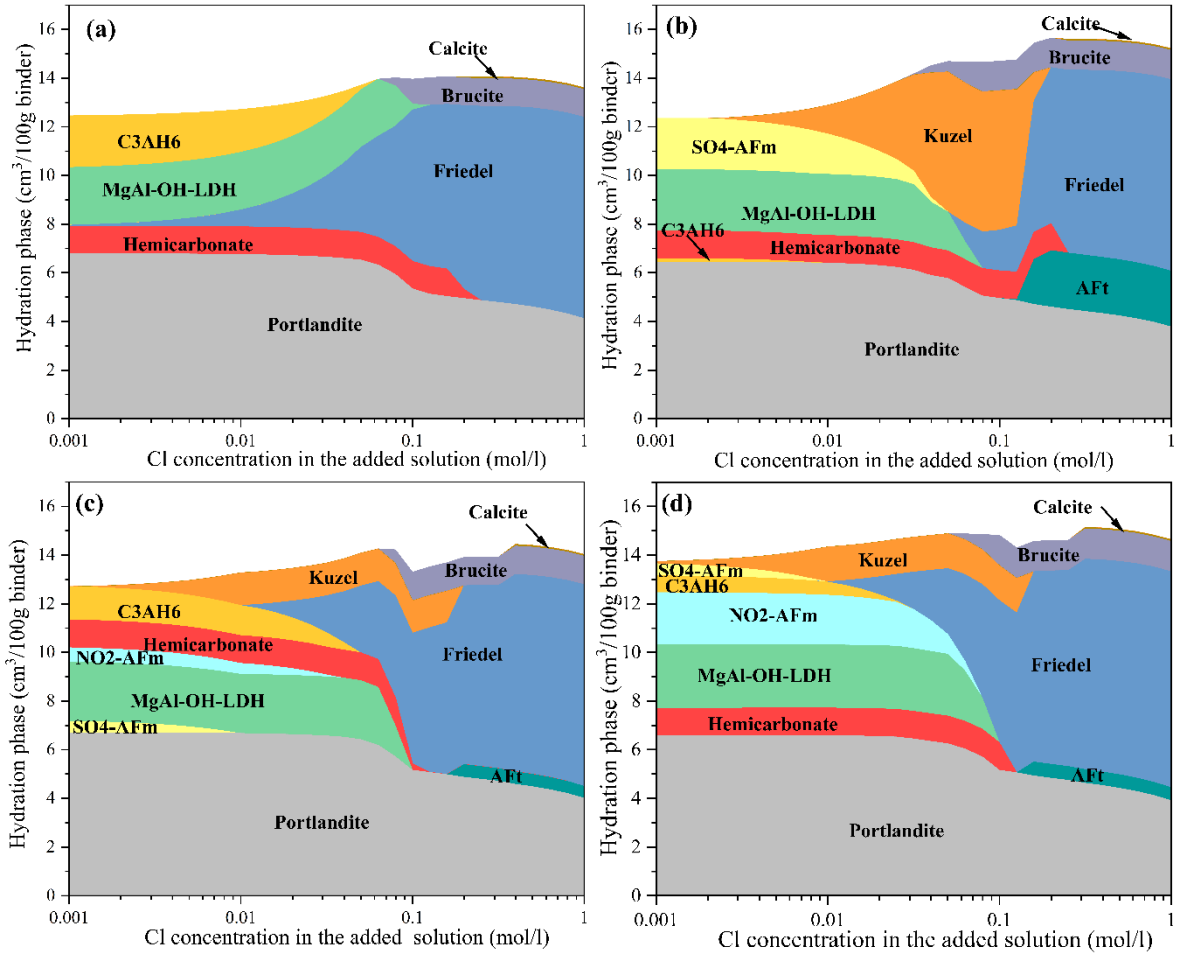
(a)
Calcite
Brucite
C3AH6
Friedel
MgAl-OH-LDH
Hemicarbonate
Portlandite
Hydration phase (cm3/100g binder)
Cl concentration in the added solution (mol/l)
(b)
Calcite
Brucite
Kuzel
SO4-AFm
Friedel
MgAl-OH-LDH
C3AH6
Hemicarbonate
AFt
Portlandite
Hydration phase (cm3/100g binder)
Cl concentration in the added solution (mol/l)
(c)
Calcite
Kuzel
Brucite
C3AH6
Hemicarbonate
NO2-AFm
Friedel
MgAl-OH-LDH
SO4-AFm
AFt
Portlandite
Hydration phase (cm3/100g binder)
Cl concentration in the added solution (mol/l)
(d)
Calcite
Kuzel
Brucite
SO4-AFm
C3AH6
NO2-AFm
Friedel
MgAl-OH-LDH
Hemicarbonate
AFt
Portlandite
Hydration phase (cm3/100g binder)
Cl concentration in the added solution (mol/l)

Fig. 10.

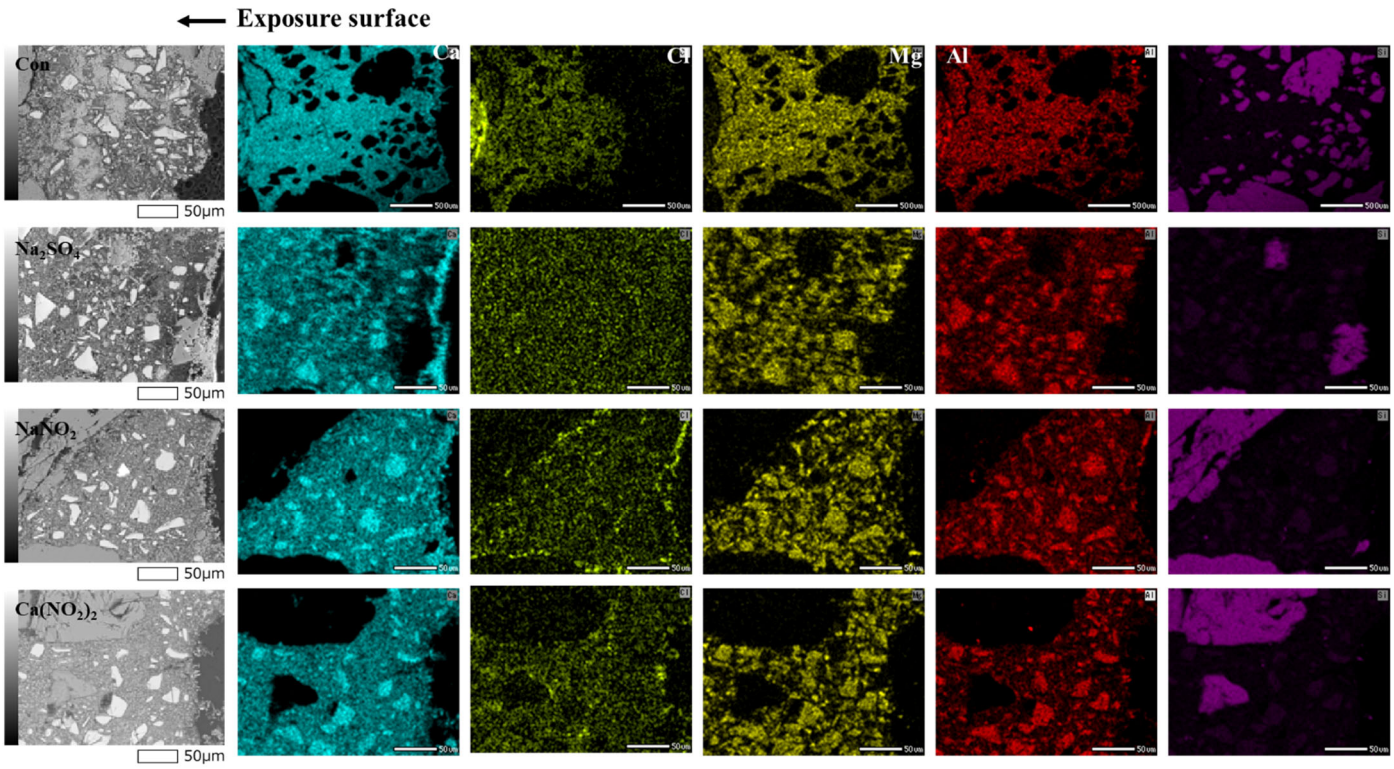

Fig. 11.

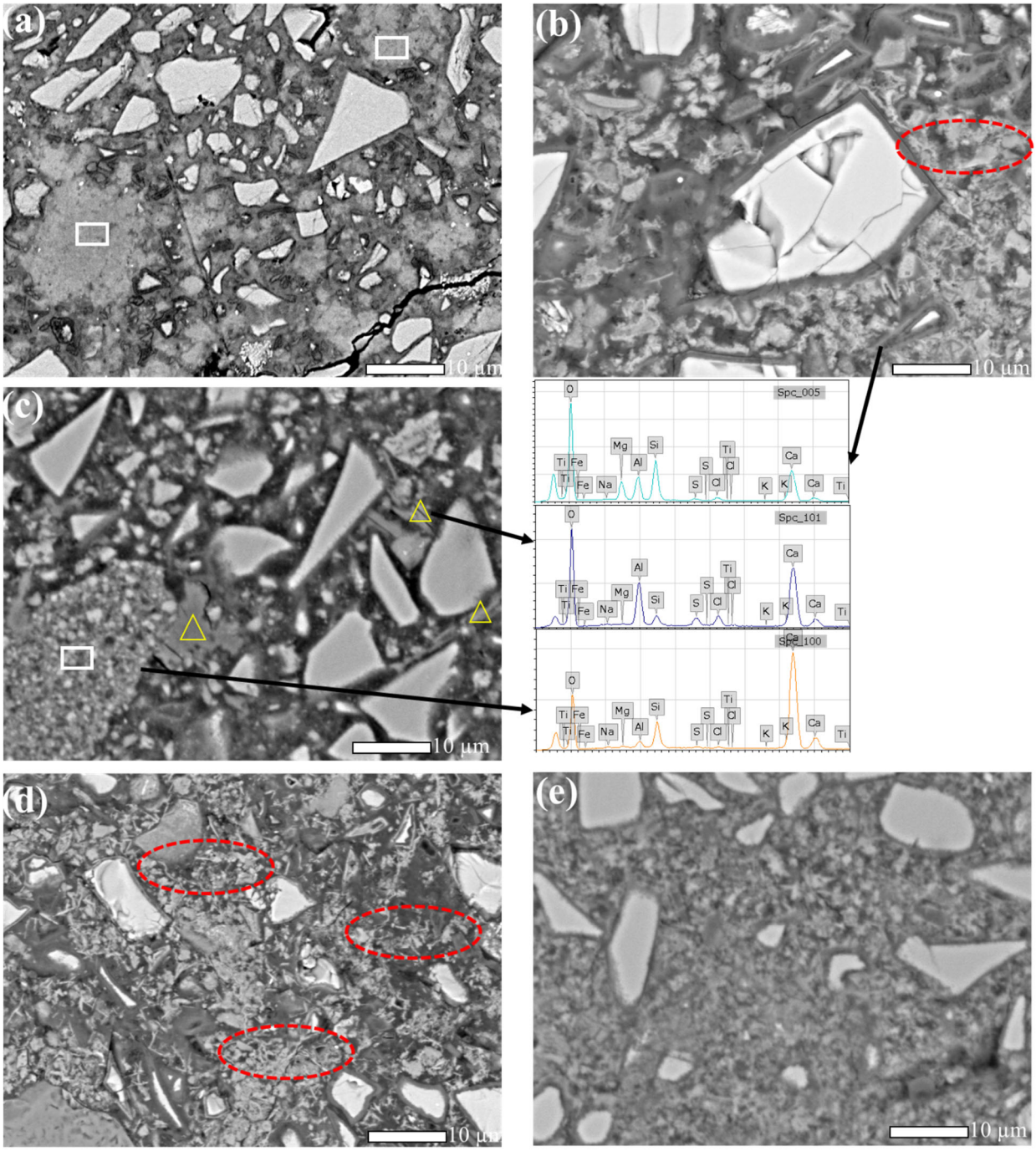
(a)
10 µm
(b)
10 µm
(c)
10 µm
Spc_005
Spc_101
Spc_100
O
Mg
Si
Ti
Fe
Al
S
Cl
Ca
Na
K
(d)
10 µm
(e)
10 µm

Fig. 12.

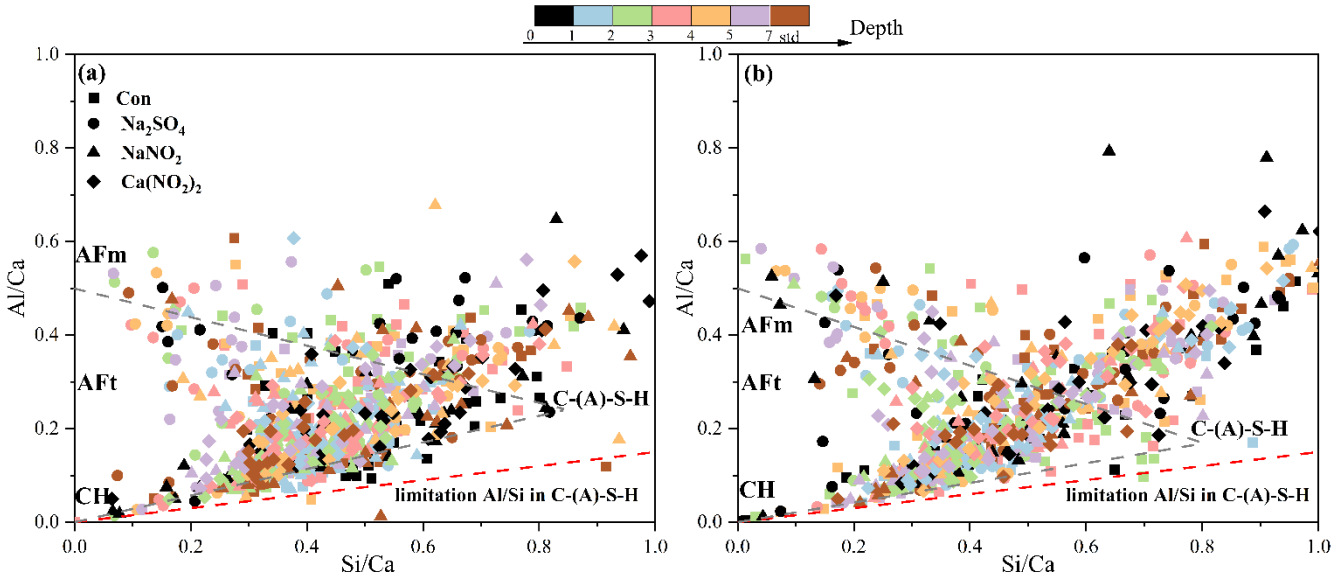
0 1 2 3 4 5 7 std
Depth
(a)
Con
Na_2SO_4
$NaNO_2$
$Ca(NO_2)_2$
AFm
AFt
CH
C-(A)-S-H
limitation Al/Si in C-(A)-S-H
Al/Ca
Si/Ca
(b)
AFm
AFt
CH
C-(A)-S-H
limitation Al/Si in C-(A)-S-H
Al/Ca
Si/Ca

Fig. 13.

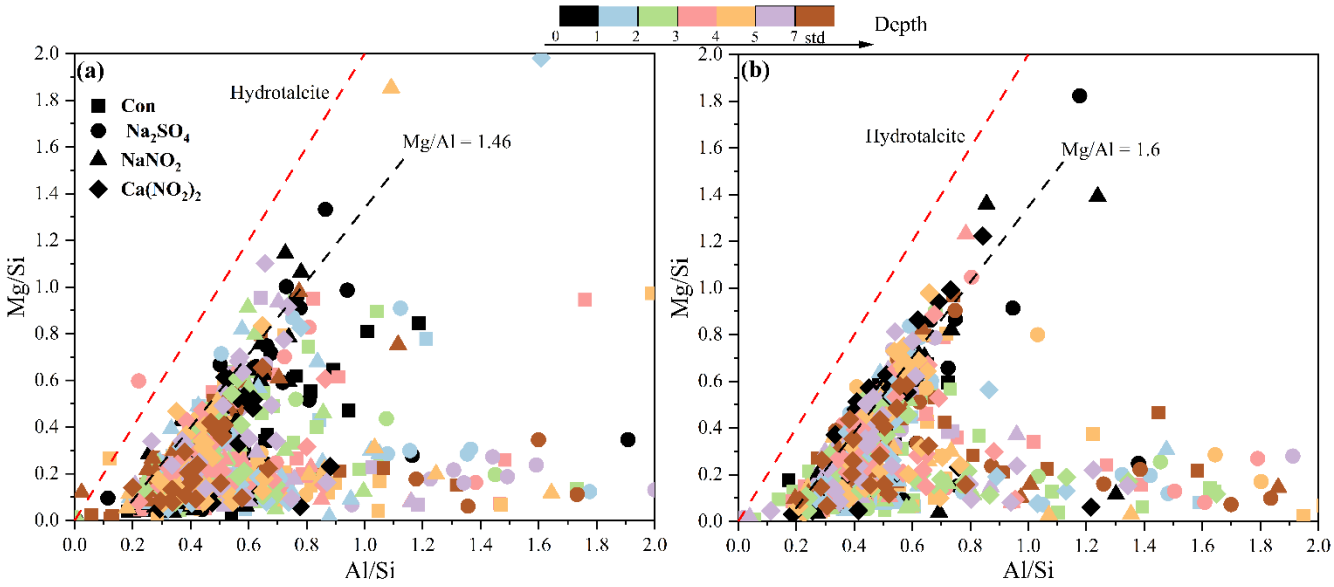
Depth
0
1
2
3
4
5
7 std
(a)
Con
Na_2SO_4
$NaNO_2$
$Ca(NO_2)_2$
Hydrotalcite
Mg/Al = 1.46
Mg/Si
Al/Si
(b)
Hydrotalcite
Mg/Al = 1.6
Mg/Si
Al/Si

Fig. 14.

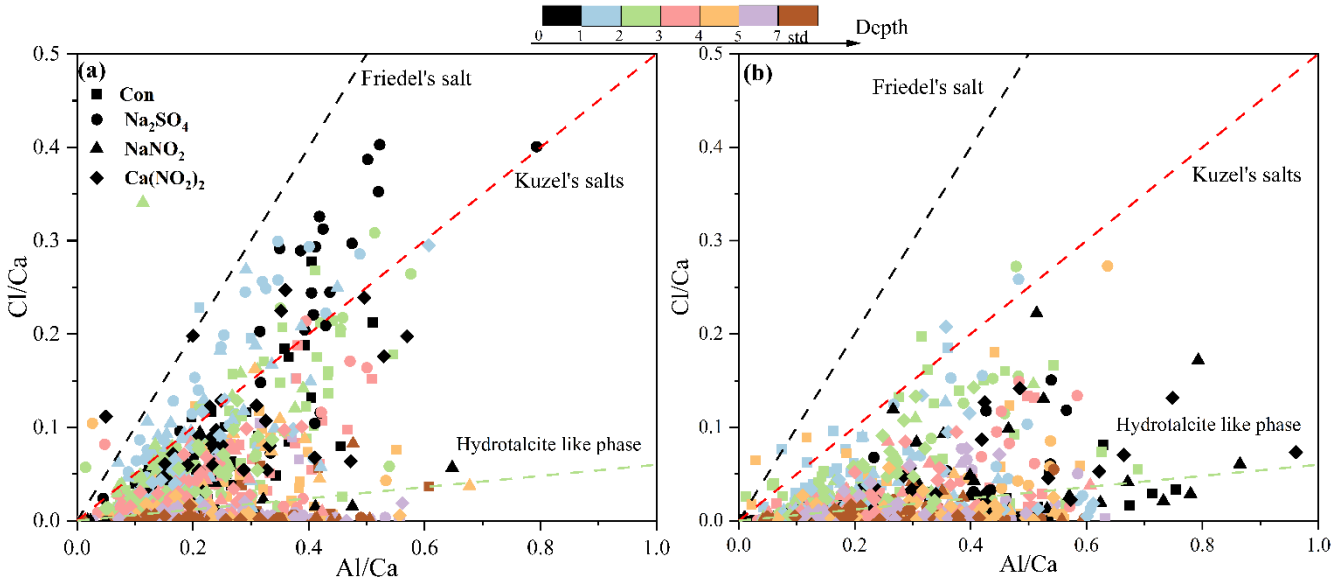
0 1 2 3 4 5 7 std
Depth
(a)
Con
Na_2SO_4
$NaNO_2$
$Ca(NO_2)_2$
Friedel's salt
Kuzel's salts
Hydrotalcite like phase
Cl/Ca
Al/Ca
(b)
Friedel's salt
Kuzel's salts
Hydrotalcite like phase
Cl/Ca
Al/Ca

Fig. 15.

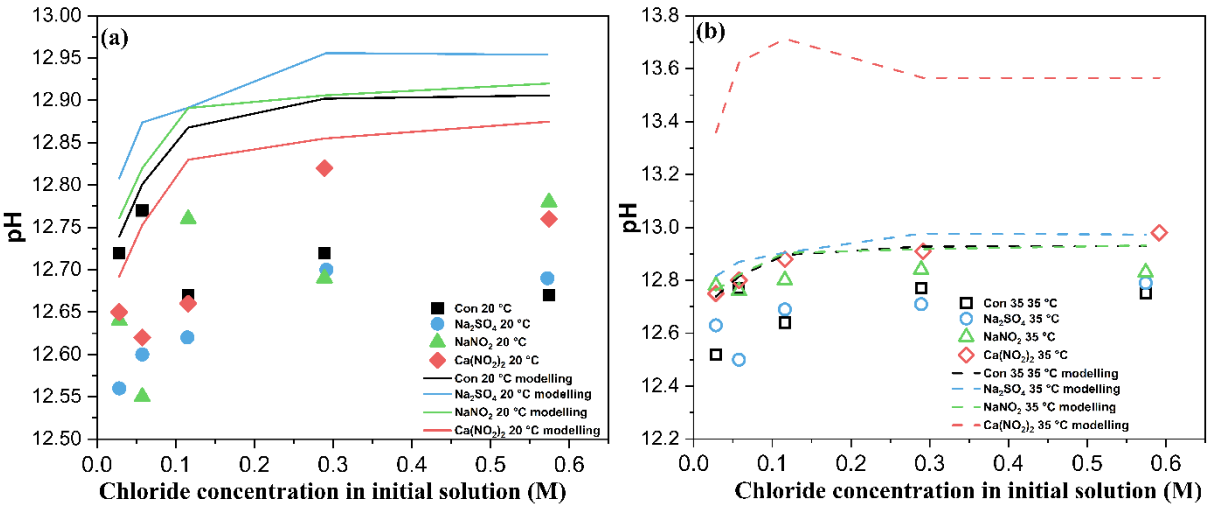
(a)
pH
Chloride concentration in initial solution (M)
Con 20 °C
Na2SO4 20 °C
NaNO2 20 °C
Ca(NO2)2 20 °C
Con 20 °C modelling
Na2SO4 20 °C modelling
NaNO2 20 °C modelling
Ca(NO2)2 20 °C modelling
(b)
pH
Chloride concentration in initial solution (M)
Con 35 35 °C
Na2SO4 35 °C
NaNO2 35 °C
Ca(NO2)2 35 °C
Con 35 35 °C modelling
Na2SO4 35 °C modelling
NaNO2 35 °C modelling
Ca(NO2)2 35 °C modelling

Fig. 16.

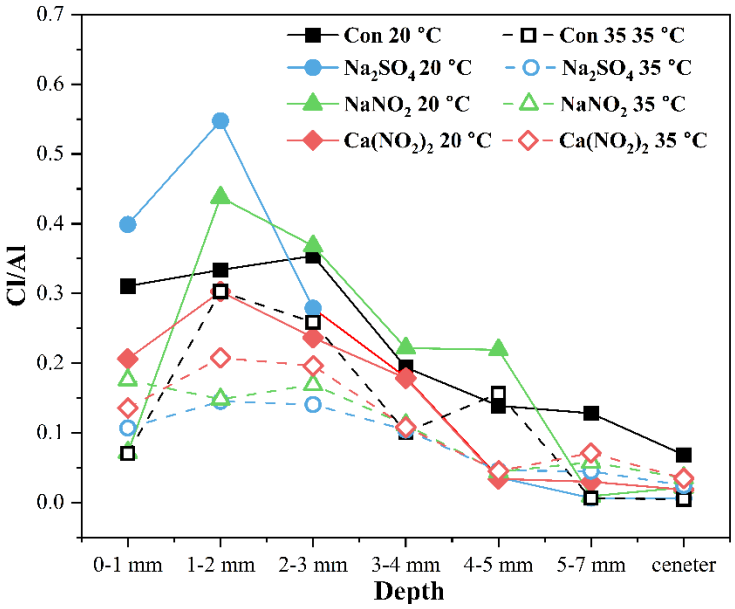
Con 20 °C
Con 35 35 °C
Na2SO4 20 °C
Na2SO4 35 °C
NaNO2 20 °C
NaNO2 35 °C
Ca(NO2)2 20 °C
Ca(NO2)2 35 °C
Cl/Al
0.0
0.1
0.2
0.3
0.4
0.5
0.6
0.7
0-1 mm
1-2 mm
2-3 mm
3-4 mm
4-5 mm
5-7 mm
ceneter
Depth

Fig. 17.

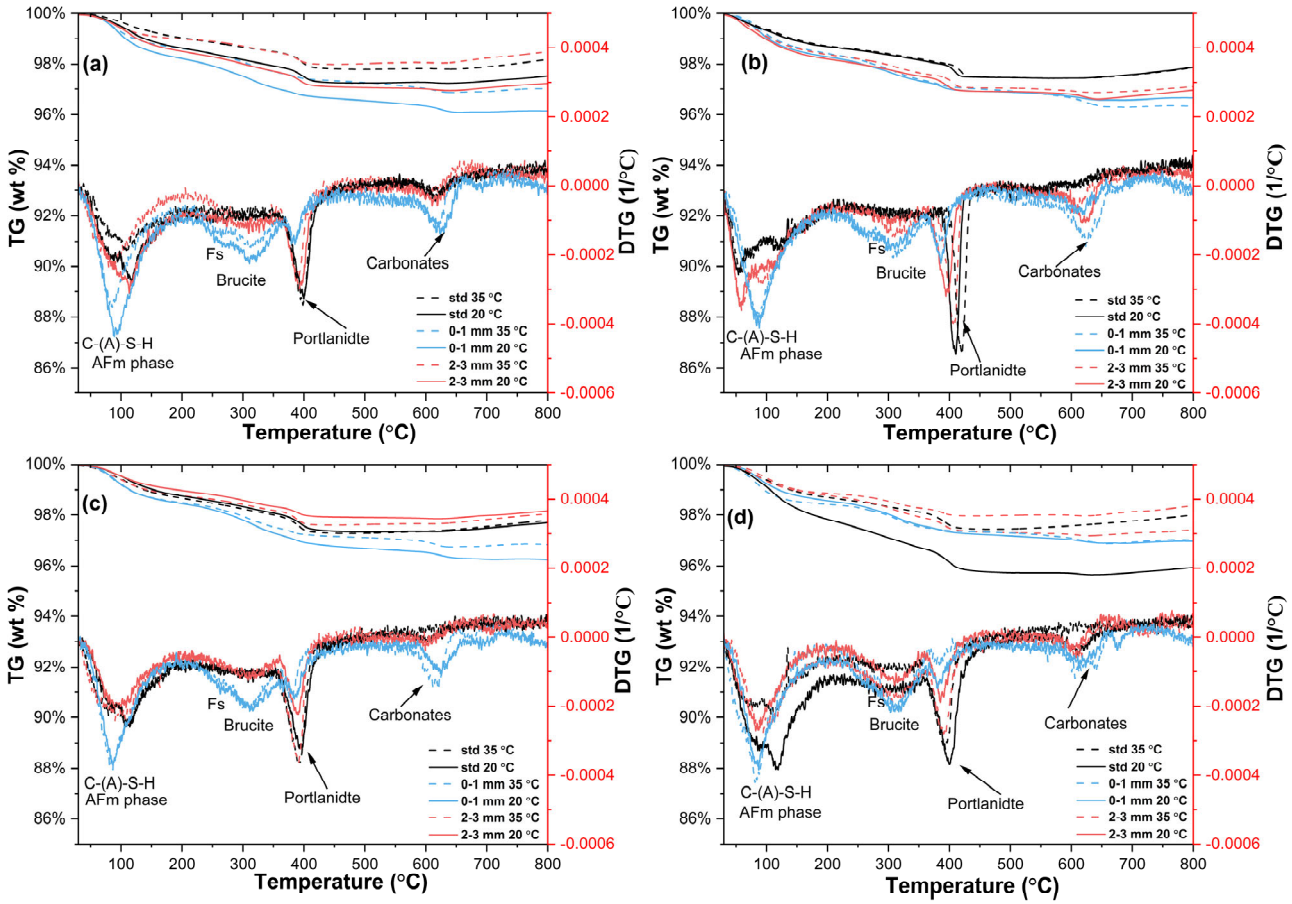
(a)
(b)
(c)
(d)
TG (wt %)
DTG (1/°C)
Temperature (°C)
C-(A)-S-H
AFm phase
Fs
Brucite
Portlanidte
Carbonates
std 35 °C
std 20 °C
0-1 mm 35 °C
0-1 mm 20 °C
2-3 mm 35 °C
2-3 mm 20 °C

Fig. 18.